



HAL
open science

On the origin of the strain hardening mechanisms of Ni20Cr alloy manufactured by laser powder bed fusion

Shubham Sanjay Joshi, Clément Keller, Lydie Mas, Williams Lefebvre, Eric Hug, Jean-Philippe Couzinie

► To cite this version:

Shubham Sanjay Joshi, Clément Keller, Lydie Mas, Williams Lefebvre, Eric Hug, et al.. On the origin of the strain hardening mechanisms of Ni20Cr alloy manufactured by laser powder bed fusion. International Journal of Plasticity, 2023, 165, pp.103610. 10.1016/j.ijplas.2023.103610 . hal-04089732

HAL Id: hal-04089732

<https://hal.science/hal-04089732>

Submitted on 5 May 2023

HAL is a multi-disciplinary open access archive for the deposit and dissemination of scientific research documents, whether they are published or not. The documents may come from teaching and research institutions in France or abroad, or from public or private research centers.

L'archive ouverte pluridisciplinaire **HAL**, est destinée au dépôt et à la diffusion de documents scientifiques de niveau recherche, publiés ou non, émanant des établissements d'enseignement et de recherche français ou étrangers, des laboratoires publics ou privés.

On the origin of the strain hardening mechanisms of Ni20Cr alloy manufactured by laser powder bed fusion

Shubham Sanjay Joshi ¹, Clément Keller ², Lydie Mas ³, Williams Lefebvre ¹, Eric Hug ³, Jean-Philippe Couzinié ⁴

¹ Groupe de Physique des Matériaux, Normandie Université, INSA de Rouen Normandie, Université de Rouen, UMRCNRS 6634, Saint-Etienne du Rouvray, France

² Laboratoire Génie de Production, INP-ENIT, Tarbes, France

³ Laboratoire CRISMAT, Normandie Université, Université de Caen, UMRCNRS 6508, Caen, France

⁴ Université Paris Est, ICMPE (UMR 7182), CNRS, UPEC, Thiais, France

Abstract

Additively Manufactured (AM) metallic alloys differ from their conventionally produced counterparts by complex multi-scaled microstructures leading to deeply modified mechanical behavior. The characterization of these new links between microstructure and mechanical properties is of first importance. Nevertheless, many alloys produced by Laser Powder Bed Fusion (LPBF) process exhibit multi-phase microstructures which makes difficult the understanding of these links. In this article, we aimed at simplifying this complexity by investigating the basic strain hardening mechanisms of AM (LPBF) alloys of a theoretically monophasic Ni20Cr alloy manufactured by laser powder bed fusion. Based on the analysis of the microstructure and the tensile mechanical behavior including loading-unloading-relaxation tests, a comparison with conventionally manufactured Ni20Cr alloy is performed. First, an increase in yield stress for the LPBF samples is observed due to both effective stress and backstress modification. Second, the strain hardening mechanisms are modified for LPBF manufactured samples compared to cast ones. Kocks-Mecking model is then employed to reproduce the tensile curves and better analyze the strain hardening mechanisms. Results are discussed in terms of specific LPBF microstructure feature contributions to stress and strain hardening. We reveal that dislocation cells associated to dendrites are proved to be responsible for about 50% of the improved yield stress of LPBF material and seem to control the dislocation production, forest interactions being inoperative for those materials.

This version is a post-print version. The edited version can be found here:

<https://doi.org/10.1016/j.ijplas.2023.103610>

Keywords: Additive manufacturing, strain hardening, microstructure, dislocations, back stress and effective stress, Kocks-Mecking formalism.

1. Introduction

Additive Manufacturing (AM) consists in a belt of techniques that produces 3D components slice by slice or more familiarly called as layer by layer manufacturing (Herzog et al., 2016) (Nezhadfar et al., 2021). Out of the many currently available techniques, Laser Powder Bed Fusion (LPBF) process is a laser assisted powder-based AM technique that specializes in metallic materials. In this process, due to extremely high cooling rates, the liquid melt track

solidifies and hardens quickly (Srinivas and Babu, 2017) (Blakey-Milner et al., 2021). The most common differences in terms of microstructure that LPBF process brings out are high initial dislocation density, solute segregation, dendritic solidification, presence of high residual stresses, morphological and crystallographic textures, distinctive melt pool features, regular or irregular shaped porosities, stable or metastable precipitates, etc. (Herzog et al., 2016). The understanding of the influence of the specific LPBF microstructure on the mechanical properties is of first importance to tailor specific microstructures and properties for a correct design of mechanically reliable metallic parts in different industrial applications.

Gorsse et al. (Gorsse et al., 2017) describe a basic two-point criterion for a metallic system to be successfully processed via LPBF: good weldability to avoid solidification cracking and input of micron-level homogeneously spherical metal powders. Special attention has been paid to the additive manufacturing of alloys that fulfil these conditions and also have great industrial interest. Hence, the alloy systems which are mostly investigated and produced are Ni-superalloys, Co-Cr-Mo alloys, steels, Ti-alloys, Al-alloys, Cu-alloys, refractory high entropy alloys, etc.

Despite the generally multi-phased character of these materials, the dependence of the mechanical behavior on basic microstructural features related to LPBF manufacturing such as melt pools, crystallographic and morphological texture, grain size, dendrite size or initial dislocation density, etc. has been investigated. Considering the melt pools, there is a consensus on the almost no direct influence of this parameter on the plastic behavior (DebRoy et al., 2018; Shifeng et al., 2014). On the contrary, the crystallographic texture clearly impacts the mechanical properties. Depending on the manufacturing strategy, i.e. applied volumetric energy and orientation between lasing planes, equiaxed grains without preferential orientations or columnar grains sharing similar orientations can be obtained (DebRoy et al., 2018; Gokcekaya et al., 2021; Hug et al., 2022; Nadammal et al., 2021; Vieille et al., 2020). In that case, cubic or Goss textures are generally reported (DebRoy et al., 2018; Gokcekaya et al., 2021; Hagihara and Nakano, 2022; Nadammal et al., 2021) inducing anisotropic mechanical behavior (influence of building direction).

At a lower scale, the grain size was also reported to influence the mechanical behavior for LPBF alloys. In particular, some researchers applied the Hall-Petch (HP) relationship to model the grain size dependence and different trends were reported. On the one hand, it has been proved that the HP relationship can be applied successfully for LPBF alloys, with either similar (Hug et al., 2022; Krakhmalev et al., 2018) or different (Mukherjee, 2019) HP constants compared to the same alloys produced by conventional methods. Independently of the HP relationship modeling, the grain size strengthening is expected to be low (Bronkhorst et al., 2019). Furthermore, for heavily textured materials with columnar grains, an effective grain size was proposed to take into account the average distance between grain boundaries alongside the mechanical loading direction (Bahl et al., 2019; Mukherjee, 2019).

At the intragranular level, dislocation cells associated to dendrite growth during solidification were reported to significantly affect the mechanical behavior. Firstly, as for texture, there is a clear consensus on the strengthening effect of dislocation cells (Krakhmalev et al., 2018; Liu et al., 2018; Wang et al., 2018; Zhong et al., 2016). HP relationship was also successfully applied using the cell size instead of the grain size suggesting similar strengthening mechanisms (Wang et al., 2018). Moreover, dedicated investigation on this microstructural feature reveals that they

are responsible for the large ductility generally observed for as-built AM alloys despite their elevated yield stress (Liu et al., 2018; Wang et al., 2018). For LPBF 316L, dislocation cells were reported to participate in strain hardening due to restrictions of the average dislocation mean free path (Bean et al., 2022). Finally, the large dislocation density of LPBF alloys, ranging between 10^8 - 10^9 mm^{-2} is also responsible for the large yield stress of those materials (DebRoy et al., 2018).

Despite the efforts of the ‘mechanics of materials’ community, the intrinsic multi-scale character of LPBF microstructure and its dependence with the manufacturing process prevented the quantitative estimation of the influence of each microstructure feature on the mechanical properties. For instance, increment in applied volumetric energy leads to a combined increase in grain size, in dislocation cell diameter and in texture index, which impede any understanding of the microstructural feature, i.e. average grain or dislocation cell diameter to be associated to the HP relationship (Wang et al., 2021). Moreover, the presence of different phases such as γ' or γ'' in Ni-based superalloys can also modify the influence of the LPBF microstructure on the mechanical properties. It is thus difficult to understand the specific role played by each LPBF microstructure at different scales on the mechanical behavior.

To improve the understanding of the basic relationship between microstructure and mechanical properties for LPBF materials, modelling can be employed. In literature, several articles using Kocks-Mecking (KM) models for mechanical behavior analysis have been published for such purpose for stainless steels (Bahl et al., 2019), titanium alloys (Bambach et al., 2021; Gallmeyer et al., 2020) and aluminum alloys (Jain et al., 2022; Zhang et al., 2021; Z. Zhang et al., 2022). In particular, this model was employed for 316L to understand the building orientation influence on the tensile curve (Bahl et al., 2019). Authors reported that differences in dynamic recovery and twinning ability is responsible of the mechanical behavior anisotropy. For LPBF processed Al-Si alloys, a lower dislocation storage for as-built samples compared to heat treated ones was reported using KM models (Jain et al., 2022). Nevertheless, regarding the role played by each microstructural characteristic (isolated dislocations, dendrites, grain size...) on the strain hardening for LPBF alloys, no sounded conclusions have been reported. Indeed, those works considered basic contribution of forest dislocation and dislocation annihilation on the strain hardening owing to other contributions such as initial dislocation structures (dendrites) or twins which have been proved to deeply influence the mechanical behavior. Other works using crystalline plasticity have been also published. Using complex 3D virtual microstructures and either empirical or physical based models, those works were able to reproduce, for instance, the effect of texture, grain morphology (Acar et al., 2022; Ghorbanpour et al., 2020) as well as anisotropy in tension/compression (Fan et al., 2021; Ghorbanpour et al., 2020). Nevertheless, no result was reported on the effect of dendrites due to the difficulty to generate polycrystalline aggregates considering the different microstructural length scales. Moreover, the absence of clear identification of the most influent internal scale on the mechanical behavior, both in terms of flow stress and strain hardening alongside with the large computation cost associated to realistic 3D microstructures, leads to the arrest of development of specific constitutive laws for additively manufactured materials.

One way to improve our knowledge about the strain mechanisms of LPBF materials is to investigate the mechanical behavior of alloys with simplified microstructures. Face-Centered Cubic (FCC) alloys without precipitation hardening and low amounts of secondary phases are ‘good candidates’ for such purpose. In that aspect, Ni-Cr binary alloy, Ni₂₀Cr (80 wt.% Ni and

20 wt.% Cr) which is widely employed industrially can be considered. Ni20Cr is mostly known for its excellent mechanical properties, enhanced electrical resistance at high temperature thanks to Ni, good corrosion resistance due to the presence of Cr (Sarantopoulos et al., 2011; Yun et al., 2021) and can be produced by LPBF (Hug et al., 2022; Song et al., 2014). A dominant FCC phase with small chromium precipitates in dendrite walls were reported in these previous works. Moreover, the addition of chromium into nickel leads to a low stacking fault energy (γ) of about 13 J/cm² (Wolf et al., 1994). The inverse of associated partial dissociation distance is proportional to the ratio of $\gamma/\mu b^2$ and was approximately calculated to be $2 \times 10^6 \text{ m}^{-1}$ (Marnier et al., 2016) leading to a very pronounced planar glide. Ni20Cr behaves in contradictory manner to 316L which exhibits very similar microstructure but enables cross-slip. Henceforth, restricted dislocation annihilation is expected for Ni20Cr. For Ni20Cr, all strain mechanisms are based on dislocation production mechanisms related to interactions between mobile dislocations and each LPBF microstructural feature without any influence of length scales (such as partial dissociation distance), which do not depend on the manufacturing process.

Hence this study is based on the experimental characterization of strain hardening mechanisms of Ni20Cr fabricated by LPBF. The objectives are to analyze and quantify the contribution of microstructural features like grain size, initial dislocation cells (dendrites), initial dislocation density in soft zones, etc. on both flow stress and strain hardening. To this aim, the mechanical behavior in tension was characterized using Loading-Relaxation-Unloading (LRU) tests alongside with the microstructure using scanning and transmission electron microscopy. These properties were then compared with those of the same alloy produced conventionally (via casting) to highlight the specificity of the strain hardening mechanisms associated with additive manufacturing. The tensile behavior of both alloys is then successfully modelled using the Kocks-Mecking formalisms to understand the relationship between the two investigated microstructural parameters and mechanical properties.

The paper is organized as follows. In a first section, the material and the experimental methods are described; then in second section, the Kocks-Mecking model employed in this study is detailed. Further, results, both in terms of mechanical behavior and microstructure characterization are proposed in a third section; and they are finally discussed in fourth section.

2. Material, experiments and methods

2.1. Material fabrication

The additively manufactured LPBF Ni20Cr samples were produced using the SLM125^{HL} machine at CRISMAT laboratory in Caen, France. The parameter set is summarized in table 1 and has been optimized in a previous study by Hug and co-authors (Hug et al., 2022) to reduce the sample porosity. In particular, the 62 J/mm³ volumetric energy give rise to a crystallographic texture free material.

Table 1: Optimized parameters used for LPBF fabrication of Ni20Cr specimens

LPBF parameters	Data
Gas velocity	7 m/s (Argon)
Laser power	200 W
Scanning speed	900 mm/s
Hatch distance	0.12 mm
Layer thickness	30 μm
Scanning strategy	Stripes (rotation angle of 67°)
Volumetric energy	62 J/mm ³

The building platform was preheated at 200°C to avoid occurrence of cold cracking due to residual stresses. Cubic samples with edge length of 20 mm were fabricated for initial microstructural characterization and density measurement using Archimedes method. Cylindrical samples of diameter 20 mm and length 100 mm were fabricated and then machined to achieve dog-bone specimens with dimensions according to the ISO-12106:2017 standard. The aforementioned fabricated cubic and cylindrical samples (in the pre-machined state) can be seen schematically in fig. 1(a) and fig. 1(b) and fabricated samples can be seen in fig. 1(c).

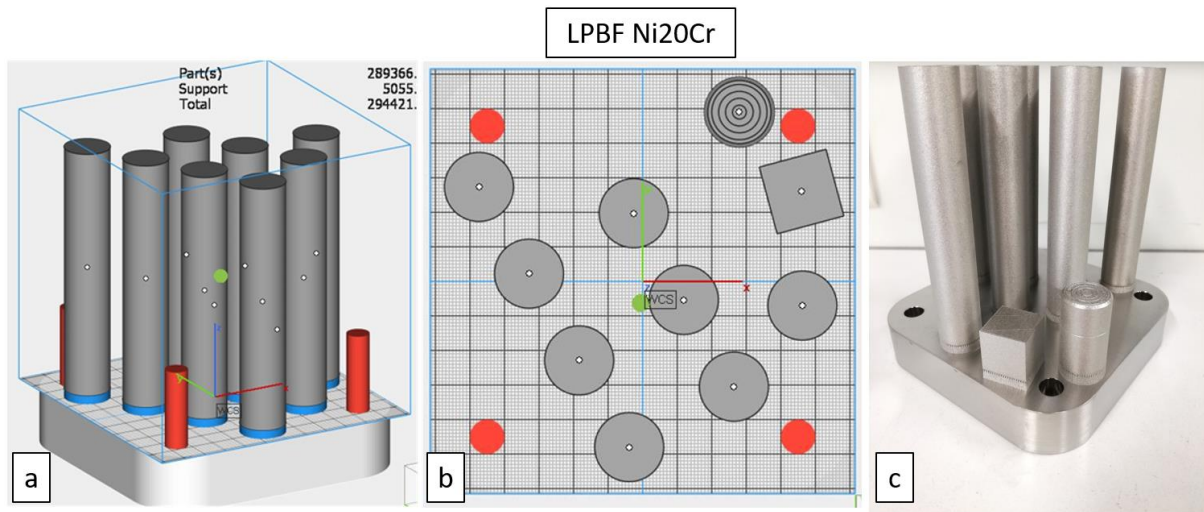


Figure 1: Schematic illustration of LPBF samples in (a) 3D model (b) top-view and (c) post fabricated build-plate.

The cast Ni20Cr samples were obtained from the provider in the machined condition with similar dimensions as mentioned above. The cast rods were cold drawn prior to machining and were completely homogenized at 1150°C for 10h to dissolve all the solidification heterogeneities and to generate an almost defect-free fully recrystallized microstructure. The homogenization temperature was selected according to the typical standards of wrought and cast Ni-based alloys in industry (Y. Zhao et al., 2021). This heat-treatment was performed in secondary vacuum with a low cooling rate (furnace switch off).

2.2. Microstructure

The microstructural characterization was done using a Scanning Electron Microscope (JEOL 7900F with Secondary Electron (SE) detector, Electron Back-Scattered Detector (EBSD), and Energy Dispersive X-Ray Spectroscopy (EDS) detector. Conventional Transmission Electron Microscope (JEOL 2000EX microscope), and Scanning Transmission Electron Microscope (JEOL ARM, an Aberration corrected Atomic Resolution Analytical Microscope) were also employed.

For the SEM, the samples were subjected to metallographic preparation starting from mechanical grinding and polishing using SiC abrasive papers followed by electropolishing in a Struers A2 electrolyte at 15 V for 30 s. Electron Back-Scattered Diffraction (EBSD) was performed to investigate both morphological and crystallographic textures as well as crystal orientation distribution analysis. A step size of 1 μm alongside with a 5° misorientation criteria for grain boundary characterization have been considered for data acquisition and treatment. Dislocations were also imaged at low magnification using SEM and Electron Channeling Contrast Imaging (ECCI) technique. Those analysis were performed at an 8 mm working distance with an acceleration voltage of 25 V associated to an electron current of 8-12 nA (read using Probe current detector) and emission current of 102.4 μA .

At high magnification, dislocations were observed by conventional TEM and Scanning-TEM (STEM). To that aim, samples were cut using precision cutting machine into 500 μm slices and were mechanically ground using SiC paper up to grit size 2400 until the thickness of 100 μm was obtained. Then thin discs of 3 mm in diameter were extracted using a punch hole device, followed by electropolishing at 24 V and -40°C using Struers TenuPol-5 (jet polishing system) with a 90% methanol and 10% perchloric acid electrolyte. This step induces a hole formation in these thin discs ensuring electron transparency. Finally, Gatan precision ion polishing system (PIPS-2) was employed for post processing of electropolished discs intended to prepare plain-view thin areas subsequent to the hole for better characterization. The milling parameters selected were 0.5 eV energy with milling angles of $\pm 3^\circ$. The acceleration voltage condition for CTEM and STEM systems was 200 kV. The probe size employed for the STEM analysis was 6C.

2.3. Mechanical tests

Monotonic tensile and Loading-Relaxation-Unloading tests (LRU) were performed on MTS servo-hydraulic machine with a load capacity of 100 kN in strain-controlled conditions with the help of a “clip-on” extensometer with the strain limit of 0.15. The strain rate employed for both kinds of tests was 10^{-3} s^{-1} . This value was set up to reduce the LRU test time without enhancing viscous effects.

For LRU, at the end of each loading sequence, the total strain is hold during 2 minutes leading to sudden stress diminution if thermally activated plastic deformation mechanisms are operating. The applied relaxation time is a compromise between overall test time and thermal stress release. This time is expected to enable more than 98% of the thermal stress release

calculated using extrapolation of curve fitting. At the end of the relaxation the stress is decreased down to 0 MPa. By ensuring a high strain rate during unloading, a mechanical quenching is expected leading to almost no changes in the microstructural features especially in dislocation density and movement keeping the same microstructural history for the next sequence (Keller et al., 2010). Such tests are hence useful to investigate the loading surface in tension, both in terms of radius and center position. In this study, a total of 21 loading-relaxation-unloading cycle sequences (hysteresis loop) were performed with an average total strain step of about 0.016. This number of sequences correspond to the apparition of necking for LPBF samples. A typical LRU sequence is displayed in fig. 2.

Finally, in order to obtain statistically significant data, multiple monotonic and LRU tests were performed for each kind of material as following:

LPBF Ni20Cr: Three monotonic and four LRU tests

Cast Ni20Cr: Three monotonic and two LRU tests.

As LRU sequences do not affect the flow stress evolution with strain, all macroscopically mechanical parameters presented on the following paragraphs (average values and error bars) are based on the analysis of all available data irrespective of the kind of mechanical tests.

2.4. Flow stress partitioning

Following literature (Mughrabi, 1983) (Dickson et al., 1984; Polák et al., 1996) (Feaugas, 1999), the flow stress (σ_{max}) can be divided into two parts namely back stress (X) and effective stress (σ_{eff}) linking to the different kinds of interactions of microstructural features with mobile dislocations (Keller et al., 2010). Back stress relates to the stress required for local straining to overcome long distance repulsive interactions of mobile dislocations with grain boundaries, heterogeneous dislocation structures or incoherent precipitates (Feaugas and Haddou, 2003). Whereas, effective stress is the stress required to move a dislocation from short range obstacles, (forest dislocations, coherent precipitates, etc.). Effective stress is then associated with the soft zones (also called matrix). As illustrated in fig. 2, back stress is a directional or kinematic component of hardening and is associated to the translation of the elastic domain (yield surface center position), whereas the latter is an isotropic component and corresponds to the radius of this domain (Doquet, 1993).

Back stress is related to long range interactions between dislocations and microstructure and can be further classified into intragranular and intergranular components (Feaugas, 1999). The former is associated with heterogeneous dislocation structures (dislocation walls or cells) whereas the latter is related to strain incompatibilities between grains. Intergranular component is supposed to be dominant at the onset of plasticity while the intragranular becomes dominant as soon as plastic strain incompatibilities (related to the difference in crystal orientation or shape) are accommodated (Feaugas and Haddou, 2003). This accommodation depends, however, on the cross-slip ability of the material. High stacking fault energy materials such as nickel or aluminum are less sensitive to the grain size as strain incompatibilities are easily accommodated by cross-slip (Feaugas and Haddou, 2003).

For viscoplastic materials, effective stress partial can further be classified into athermal (σ_{μ}) and thermal stresses (σ^*). The thermal stress partial is connected to the viscous behavior and is

associated with thermal gliding mechanisms (Feaugas, 1999; Keller et al., 2010). The quantification of all these partials is based on Dickson's method (C. Zhao et al., 2021) and requires the estimation of the reverse yield stress (σ_r) which is computed in the unloading portion of the hysteresis loop linked to loading-unloading-relaxation tests with a specific plastic strain offset (10^{-4} in this study). Based on the reverse yield stress (σ_r), flow stress (σ_{max}) and thermal stress (σ^*), relaxed during the relaxation step, effective stress and backstress can be estimated, for each relaxation-unloading sequence, using eq. 1 and eq. 2, respectively.

$$\sigma_{eff} = \frac{(\sigma_{max} - \sigma_r)}{2} - \frac{(\sigma^*)}{2} \quad (1)$$

$$X = (\sigma_{max} - \sigma_{eff}) \quad (2)$$

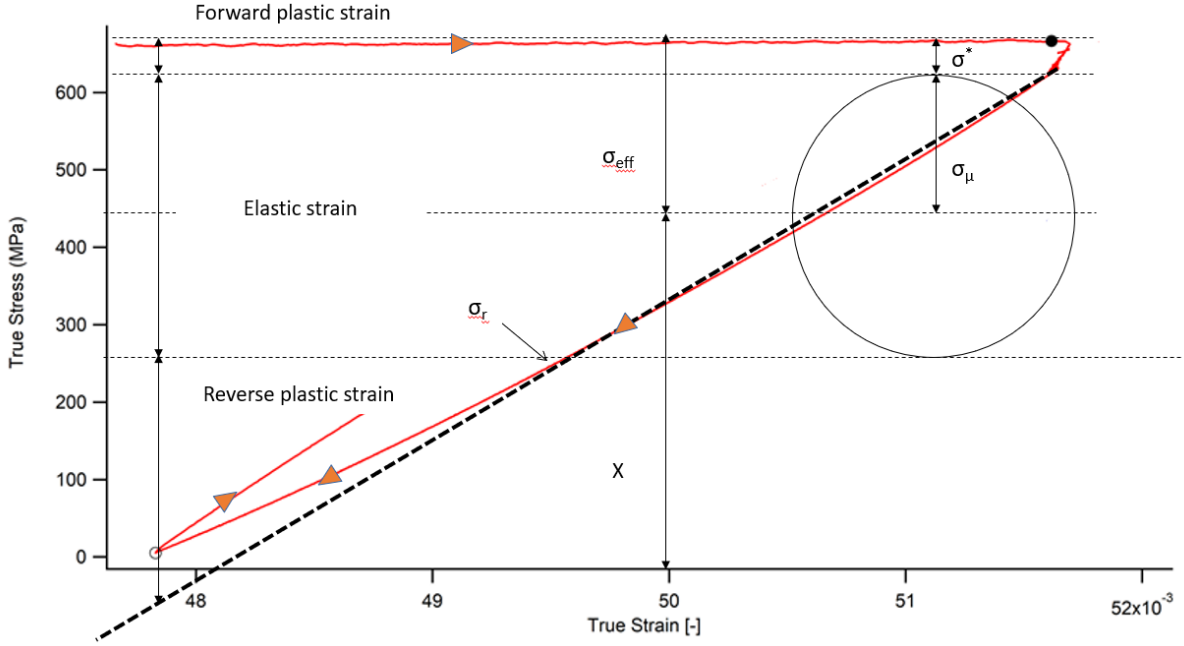


Figure 2: Illustration of an unloading sequence and flow stress partial contributions on the yielding surface. The orange colored arrows depicted on the tensile curves indicates the stress-strain direction during the test.

2.5. Activation volume

Physically, the activation volume is associated to the macroscopic sensitivity of viscoplastic flow brought about by stress application (Feaugas, 1999) and can be understood as free volume that mobile dislocations can travel under thermal activation between two thermally activated events (Keller et al., 2010).

For polycrystals, the activation volume can be expressed following eq. 3 (Feaugas, 1999) with M the Taylor factor, b the Burgers vector modulus, k_B the Boltzmann constant, T is the testing temperature and σ^* is the thermal stress. The value of the activation volume is expressed in b^3 .

$$V = M \frac{k_B T}{b^3} \left(\frac{\partial \ln \dot{\epsilon}}{\partial \sigma^*} \right) \quad (3)$$

3. Kocks-Mecking model description

When it comes to the analysis of the strain hardening mechanisms, analytical models based on dislocation densities can provide valuable information complementary to mechanical tests or microstructure observations. In this framework, Kocks-Mecking (KM) based models were successfully employed for conventional FCC alloys in the past years to reproduce and understand the strain hardening mechanisms (Kocks and Mecking, 2003; Mecking et al., 1976). The scalar character of the model and the possibility to consider the influence of several microstructural features on strain hardening, i.e. forest dislocations, grain boundaries, initial dislocation structures or precipitate networks as well as sinks such as free surfaces, make it suitable for the analysis of the mechanical behavior without need of finite element modelling associated to crystalline plasticity models.

The first constitutive equation of the Kocks-Mecking formalism relates the flow stress, σ , with the dislocation density ρ following the Taylor relationship (Kocks and Mecking, 2003):

$$\sigma = \sigma_0 + \alpha \mu b M \sqrt{\rho} \quad (4)$$

Here, M is the Taylor factor, b the Burgers vector magnitude, μ is the shear modulus and α is a material parameter considering the dislocation arrangement and the different kinds of interactions between slip systems (Lomer Cottrell locks, Hirth locks, glissile junctions...). σ_0 is an initial stress value which can be introduced to take into account the contribution of stress of secondary phases or solid solution hardening. In the case of Ni20Cr, this term will be mostly related to former contribution to the flow stress. ρ represents the average dislocation density.

The second constitutive equation is the evolution rate of the dislocation density with plastic strain. This equation, introduced by Essmann and Mughrabi (Essmann and Mughrabi, 1979), initially consisted of two terms, one related to the dislocation storage due to dislocation interactions and a second one linked to the dislocation annihilation processes (by dislocation climb or cross-slip). In the last decades, improvements of the KM model were proposed to this specific equation considering other microstructural features' contributions to strain hardening (Essmann et al., 1968; Kuhlmann-Wilsdorf, 1989; Mecking, 1975; Mecking and Kocks, 1981; Narutani and Takamura, 1991; Smallman and Ngan, 2007; Steinmetz et al., 2013). Hence, this equation can be written as the sum of six different terms following eq. 5:

$$\frac{d\rho}{d\varepsilon_p} = \frac{M\sqrt{\rho}}{\beta b} + \frac{Mk_g}{bd} + \frac{M}{bl_0} - K_2\rho - \frac{M}{bs} + \frac{1}{2eb} \cdot \frac{f_{tw}}{(1-f_{tw})} \quad (5)$$

The first term on the right-hand side is related to the athermal storage of dislocations. In that case, β represents the ratio between the mean free path of gliding dislocations L and the average dislocation distance l , assumed to be equal to the inverse of the square root of dislocation density. β is then introduced to take into account the fact that a dislocation may travel over a distance larger than the average space between dislocation. It is significant to mention that all forest dislocation interactions do not immobilize mobile dislocations.

The second term represents the contribution of grain boundaries to the strain hardening due to the geometrically necessary dislocations (GNDs) created to accommodate strain incompatibilities between grains (Ashby, 1970). This contribution is characterized by the constant k_g linked, among others parameters, to the grain shape and stacking fault energy (Gil

Sevillano, 1993). This second term is supposed to be dominant at the beginning of plasticity when strain incompatibilities between grains are important.

The third term is related to the presence of initial dislocation structures generated during previous forming processes or to a precipitate network. In this term, l_0 represents the characteristic dimensions of the initial dislocation structures or the average distance between precipitates.

The fourth term is associated with the third stage of hardening linked to the annihilation of dislocations due to cross-slip or climb during dynamic recovery (Essmann and Mughrabi, 1979; Feaugas, 1999; Kubin et al., 2009). K_2 is the rate of the annihilation process. This parameter is linked to the dislocation annihilation distance which depends on the SFE of the material, on the temperature and on the stress level.

The fifth term governs the rate of dislocation annihilation due to free surfaces as initially formulated by Mecking (Mecking, 1975) and then employed in literature to investigate surface effects for Ni multicrystals (Keller and Hug, 2017a). This rate is governed by the average distance between free surfaces s .

The last term is introduced to take into account the contribution of mechanical twinning on strain hardening (Bahl et al., 2019; Steinmetz et al., 2013). In that term, e denotes the twin width and f_{tw} the twin fraction which is supposed to depend on plastic strain. This term is restricted to low stacking fault energy alloys.

These two equations, eq. 4 and eq. 5, form the conventional one-internal variable (i.e. ρ) KM model employed in the following sections to investigate the microstructure contribution to strain hardening. To solve this system of non-linear differential equations, a script using the Opensource software Scilab was implemented to compute the numerical tensile curve using a square root optimization process (Fourth order Range Kutta method) between the experimental data and the numerical tensile curves. For the optimization process, the root mean square deviation is minimized. This minimization process takes into account the flow stress values and associated strain hardening rate. As this parameter is larger than the stress level, the strain hardening rate influence on the identification is larger compared to the stress level one and must help to accurately investigate the strain hardening mechanisms (Keller and Hug, 2017a).

4. Results

4.1. Initial microstructure (dislocations, dendrites and texture)

Fig. 3(a) and fig. 3(c) show SEM micrographs of LPBF specimens for surfaces normal to the building direction (XY plane), and fig. 3(b) and fig. 3(d) show the micrographs of homogenized cast Ni20Cr. For LPBF, a heterogenous grain sized microstructure was found as seen in fig. 3(a), whereas at the same scale, fig. 3(b) shows large grains with a completely different overview for cast. Fig. 3(c) displays parallel walls associated to dendritic solidification with significantly higher number of dislocations, as imaged by ECCI. Dislocations are also seen to be crossing these walls and tangled between them (see red circle in fig. 3 (c)). In contrast, Cast Ni20Cr microstructure illustrated in fig. 3(d) presents a clear and defect-free micrograph.

The dendrites found in LPBF specimens were analyzed and the average value of dendritic primary arm spacing (λ) was found to be $0.47 \mu\text{m}$ with subsequently calculated process cooling rate (\dot{T}) was $(2.78 \pm 0.85) \times 10^6 \text{ ks}^{-1}$ using eq. 6 (Dehoff et al., 2015), in agreement with literature (Hug et al., 2022).

$$\lambda = 97\dot{T}^{-0.36} \quad (6)$$

The possible dendritic solidification in cast was dissolved in the heat treatment to form a homogeneous microstructure. Error values shown in the cooling rate calculation has been computed using confidence interval of 95% (Ulm, 1990).

Fig. 3(c) also illustrates the segregation of Cr-rich particles (Hug et al., 2022) owing to the non-equilibrium nature of additive manufacturing. Those precipitates are mainly localized in the dendrite walls as marked by blue arrows in fig. 3(c) and scarcely in the soft zones. Energy dispersive spectroscopy (EDS) analysis over STEM of these particles revealed the presence of Cr-rich oxides with clear absence of Ni as marked in fig. 3(e).

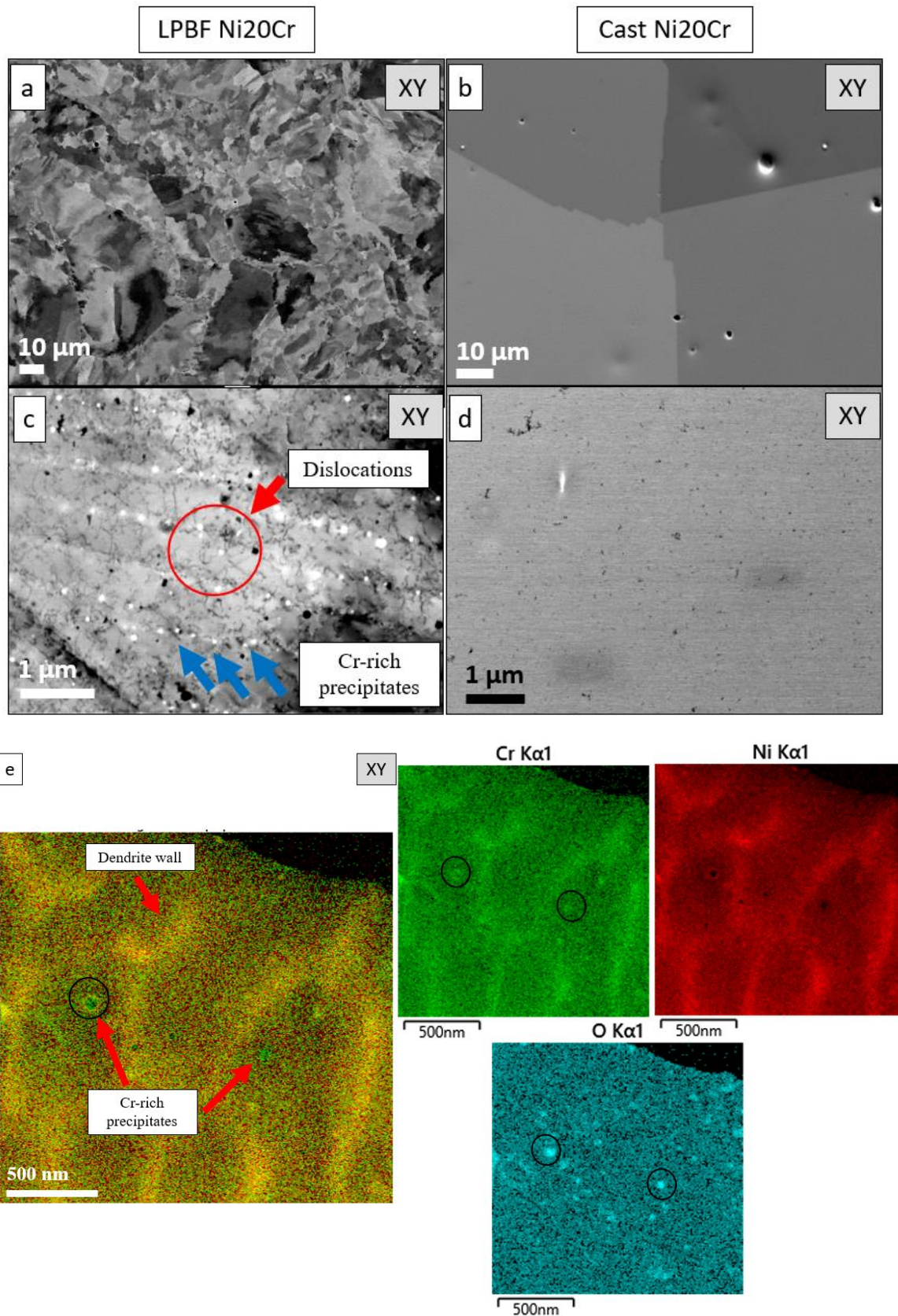


Figure 3: General initial grain structure in XY plane for (a) LPBF, (b) Cast respectively; Initial dislocation structures for (c) LPBF and (d) cast; (e) Characterization of Cr-rich particles in LPBF Ni20Cr using Energy dispersive spectroscopy (EDS) analysis over STEM. Manufacturing direction for both processes is perpendicular to the image planes.

Inside dendrites, in the soft zones, dislocation imaging of as-built LPBF samples done using STEM as shown in fig. 4(a) and fig. 4(b). Different sub-features of dislocation system like stacking fault tetrahedra, and dislocation dipoles are observed. Stacking fault tetrahedra as the most general type of vacancy clustered defects found in FCC structured metals and alloy systems (Kiritani, 1997) and generally formed in quenched or irradiated ones (Kiritani, 1997; Kojima et al., 1989; Singh et al., 2004). Here the size of the stacking fault tetrahedra lies between 10 and 50 nm and are homogeneously distributed in the material. As already seen for cast material, no such sub-features are found due to the fully recrystallized character of this material.

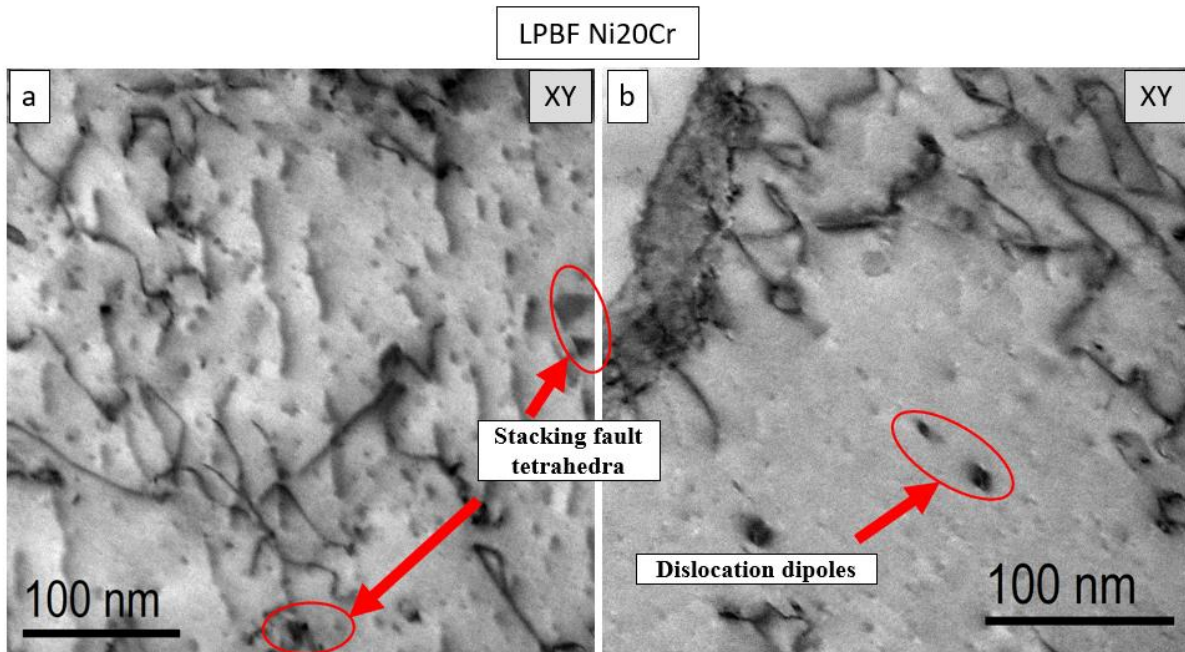


Figure 4: STEM Bright field micrograph of initial dislocation features inside dendrite (soft zones) in LPBF specimen in XY plane showing (a) Stacking fault tetrahedra, and (b) Dislocation dipole.

Electron Back-Scattered Diffraction analysis (fig. 5) shows grain orientation maps, pole figures, Kernel average misorientation maps and grain orientation spread maps for both kind of samples (perpendicular to the sample axis). For LPBF, (fig. 5(a)), grains are almost equiaxed with a low maximum intensity of pole figure of about **2.598** for the XY plane (plane perpendicular to the building direction) as seen in fig. 5(c). Similar values (**2.636**) were found for the YZ plane (plane parallel to the building direction, not shown here), indicating that there is no crystallographic texture for Ni20Cr produced by LPBF.

Grain orientation maps, inverse pole figure maps, texture intensity maps, Kernel average misorientation maps, grain orientation spread maps for XY plane have been included below in fig. 5.

Such grain structure was already reported in the case for LPBF of Inconel 718 (Vieille et al., 2020), whereas Inconel 625 via LPBF showed higher maximum intensity indicating a crystallographic texture (Beese et al., 2018). However, this texture emerging is also a function of input volumetric energy, hence comparison of texture behavior across different materials needs comparative energy. On the contrary for cast samples of Ni20Cr, huge grains are observed (fig. 5(b)) with a relatively higher maximum intensity of pole of **7.1**. Cast Ni20Cr

Electron Back-Scattered Diffraction micrograph also shows the presence of numerous annealing twins (fig. 5(b)).

When it comes to the LPBF specimens, residual stresses can be expected due to the large misorientation distribution (Kelly et al., 2021). KAM maps indicate presence of misorientation close to grain boundaries for LPBF Ni20Cr specimen as shown in fig. 5(e). Whereas fig. 5(f) shows lack of misorientation in annealed cast specimens supporting information provided by GOS analysis. Further extension of Electron Back-Scattered Diffraction analysis reports the maximal grain orientation spread (GOS) values for LPBF to be 6.8° against a value of 0.6° for cast specimens as given in fig. 5(g) and fig. 5(h). Grains with $GOS \leq 2^\circ$ are categorized as recrystallized (Field et al., 2007) hence indicating the complete recrystallization in the case of cast specimens.

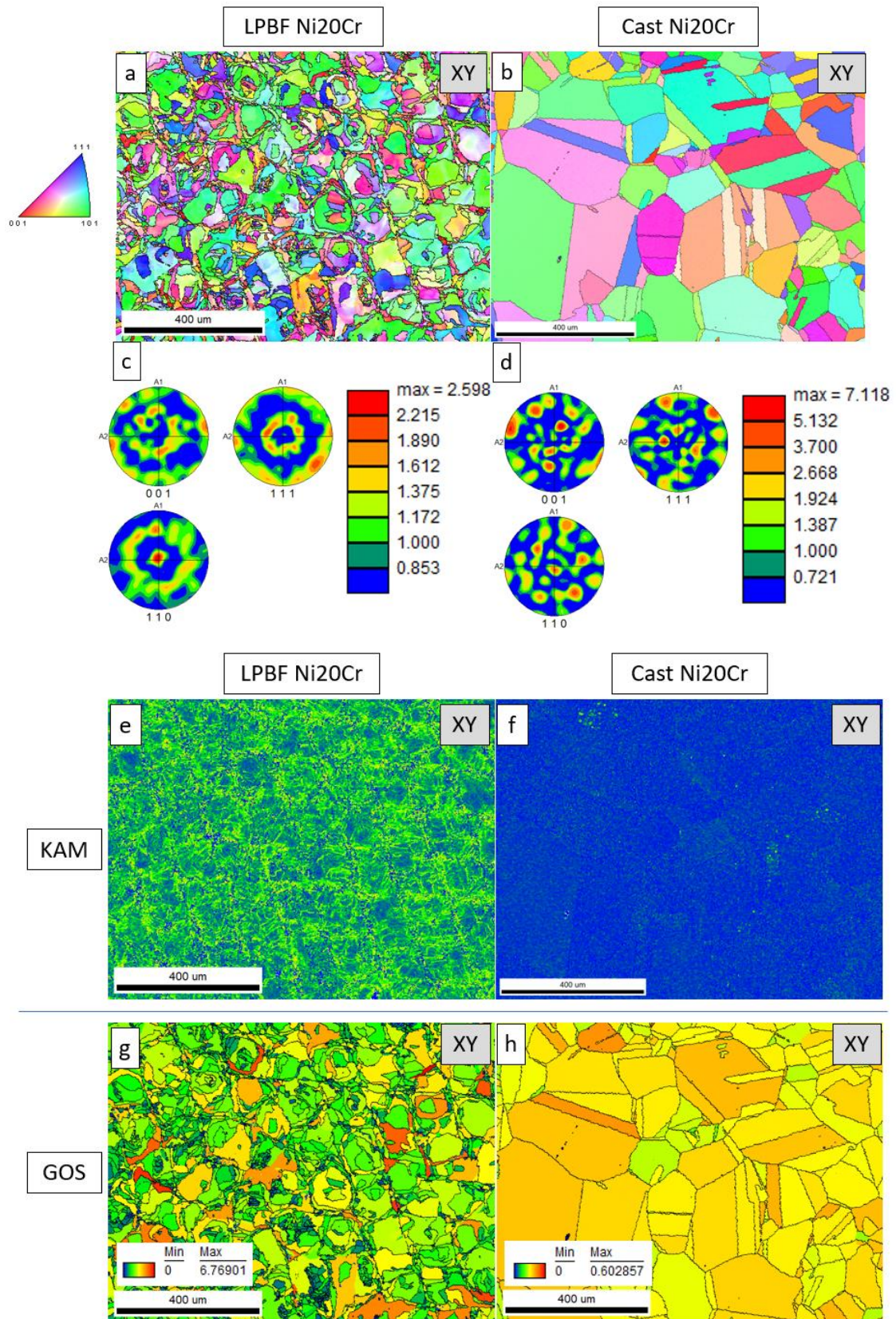


Figure 5: Initial grain orientation maps in XY plane for (a) LPBF and (b) Cast; associated pole figures between (c) LPBF and (d) Cast Ni20Cr; associated Kernel average misorientation (KAM) maps for (e) LPBF and (f) Cast; and Grain orientation spread (GOS) maps for (g) LPBF and (h) Cast Ni20Cr specimens.

The average grain size computed by Electron Back-Scattered Diffraction analysis is 70 μm for LPBF samples versus 400 μm for cast ones as illustrated in fig. 6(a).

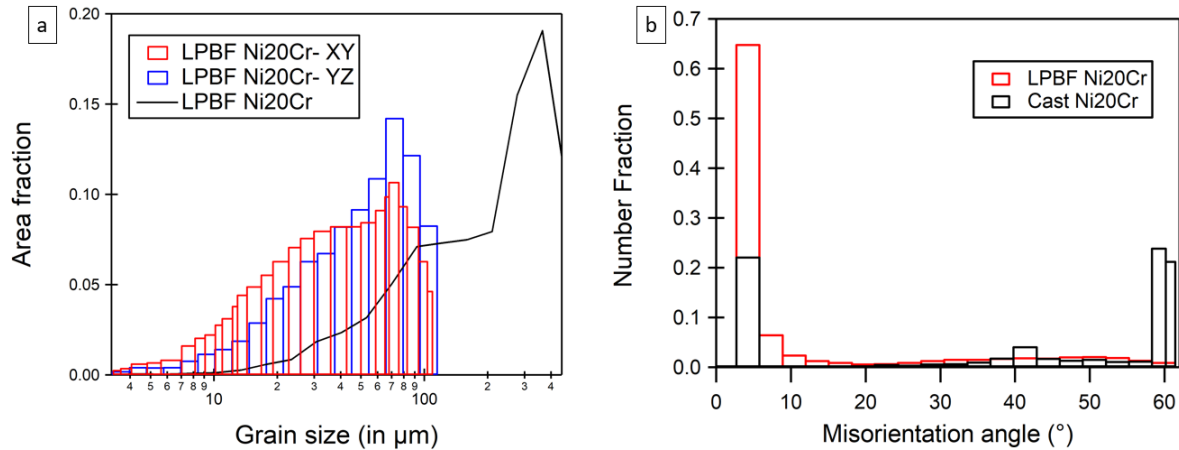


Figure 6: (a) Grain size distribution against area fraction for LPBF specimens in building direction (Z), perpendicular to the building direction (XY) and cast specimens; (b) Misorientation distribution against number fraction in LPBF and Cast Ni20Cr showing the fraction of LAGBs, HAGBs and twins.

Additionally, as depicted in fig. 6(b), a larger fraction of low angle grain boundaries (misorientation angle less than 15 $^\circ$) is observed for LPBF compared to cast (76% versus 22%) An opposite trend is observed for high angle grain boundaries, especially twins (60 $^\circ$ misorientation). Indeed, for cast, 20% of grain boundaries are assumed to be twins whereas this value is almost null for LPBF samples, in agreement with the grain orientation maps illustrated in fig. 5(a) and fig. 5(b).

4.2. Monotonic tensile behavior

The comparison of the tensile curves between cast and LPBF samples is provided in fig. 7. Out of the multiple monotonic and LRU tensile tests done on LPBF and cast samples, only one stress-strain curve for each type was selected and shown in that figure. Fig. 7(a) shows that, as expected, the LPBF samples exhibit larger flow stress than cast. Such difference is still observed using the true stress and true strain formalism (see fig. 7(b)) but, in that case, ultimate tensile strength is increased for cast due to its larger necking strain. Table 1 summarizes the yield stress (YS), ultimate tensile strength (UTS) and necking strain for LPBF and cast samples alongside with values extracted from literature, standard deviation values are shown in parenthesis in the following table. Engineering yield stress in LPBF (554 MPa) is more than three times higher than in cast condition (267 MPa), whereas significant increment in UTS (708 MPa) in LPBF samples is observed if compared to cast (662 MPa). The strength found in this study with optimized manufacturing parameters has similar or higher values than those from the literature for the same manufacturing process (Hug et al., 2022; Song et al., 2014). Marginal difference in engineering fracture strain values was observed whereas necking strain is significantly affected by the manufacturing process. Necking starts just above 22% engineering strain (indicated by blue arrow) whereas beyond 55% for cast (indicated by grey arrow).

Table 2: Summary of the monotonic tensile properties (in the engineering framework) of LPBF and cast Ni20Cr specimens in this study and comparison with literature.

Specimen	YS (MPa)	UTS (MPa)	Eng. fracture strain	Young's modulus (GPa)
LPBF (this study)	554 (9)	708 (8)	0.56 (0.10)	218 (3)
Cast (this study)	267 (44)	662 (45)	0.93 (0.11)	191 (3)
LPBF (Hug et. al.) (Hug et al., 2022)	533 (5)	671 (15)	0.35 (0.08)	195 (1)
LPBF (Song et. al.) (Song et al., 2014)	205-210	318-365	0.05	190
Strip roll casting (Das et. al.) (Das et al., 2010)	194	381	0.19	190

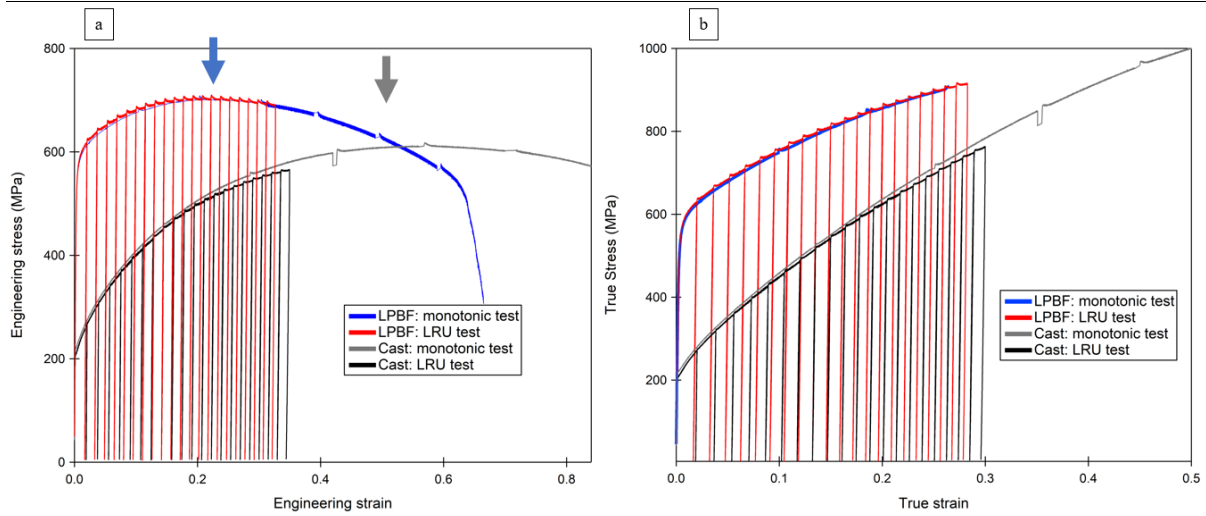


Figure 7: (a) Engineering Stress-Strain curves. (b) True Stress-Strain curves for LPBF & Cast Ni20Cr (three monotonic curves and one LRU curve have been shown for both kinds of samples).

True stress and true strain have been employed for LRU analysis and Kocks-Mecking modelling, hence respective true strain true stress data for monotonic test for LPBF and Cast Ni20Cr has been given for comparison in table 3. Notably high degree of strain hardening is seen in cast unlike in LPBF specimens. Small fluctuations visible in the stress-strain curves belong to forced unloading and loading occurred due to manual reset and re-clipping of extensometer after attainment of its maximum limit. It can be also observed in fig. 7(b) that LPBF sample exhibit non-linear hardening contrarily to cast with an almost linear hardening in agreement with the strong planar glide of this material.

Table 3: Summary of the mechanical properties in tension expressed in true stress - true strain framework for LPBF and Cast Ni20Cr.

Specimen	True YS (0.2%) (MPa)	True UTS (MPa)	True fracture strain	True necking strain
LPBF	554 (9)	902 (10)	0.51 (0.1)	0.23 (0.02)
Cast	267 (40)	1099 (28)	0.66 (0.02)	0.39 (0.05)

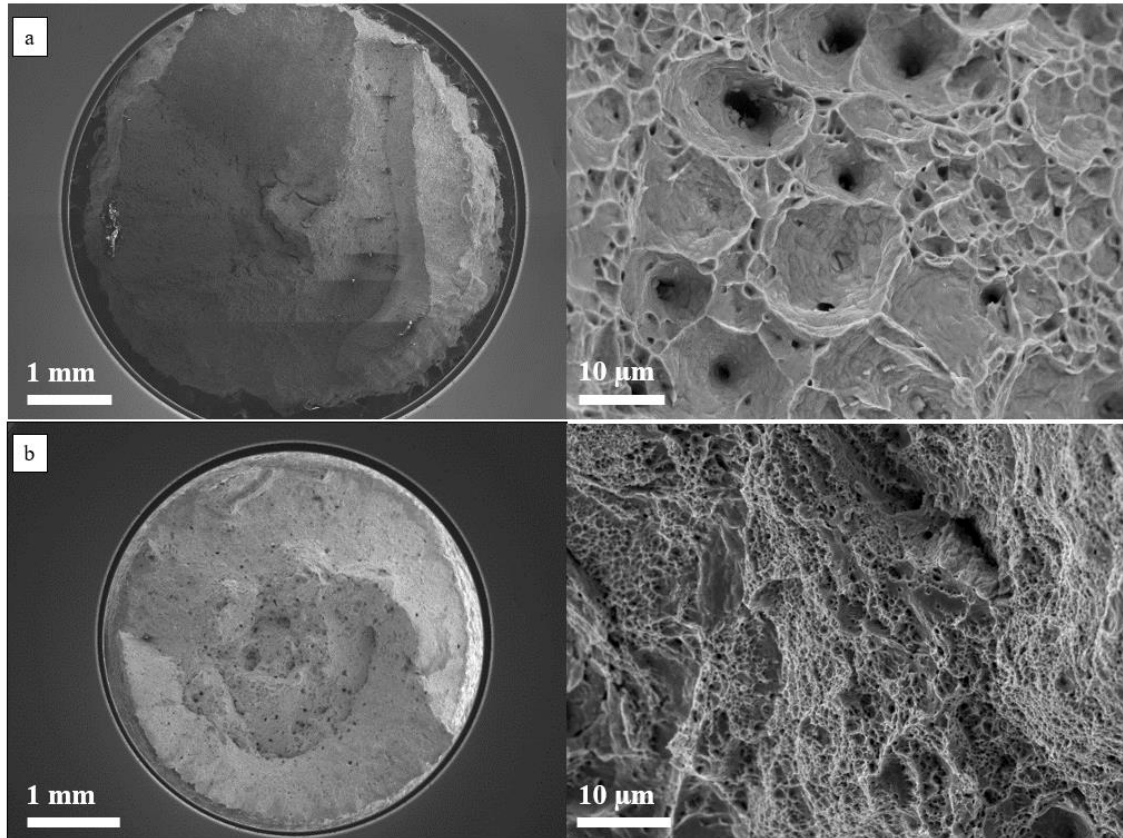


Figure 8: SEM observation of the fracture surfaces for (a) Cast Ni20Cr and (b) LPBF Ni20Cr.

Fig. 8 also shows fracture surfaces of both kinds of tested specimens having conventional cup-and-cone shaped necking zones with dimples implying the presence of ductile mode of fracture, also confirmed by other studies (Song et al., 2014). The dimples found on LPBF specimens are much finer than that of the cast specimens. Moreover, the nucleation sites for fracture in cast specimen seems to be micro pores or inclusion particles (Pantazopoulos, 2019). Similar fracture properties have been shown in the studies of other LPBF Ni-alloys (Keller et al., 2021).

4.3. Loading-Relaxation-Unloading test analysis

The loading-relaxation-unloading tests were carried out on LPBF and cast specimens till close to 30% true strain, which corresponds to the region just before necking for LPBF. Yield stress and strain hardening for both samples are very similar to those characterized using conventional tensile tests presented in the previous section.

Based on those LRU tests, the stress components partition reported in the former section has been applied to both kind of samples in order to estimate the back stress, effective stress, athermal stress, and thermal stress evolutions with strain.

Back stress (X) evolution can be seen in fig. 9. X shows higher initial value for LPBF than that of Cast, whereas the degree of hardening is higher in cast than in LPBF. The total increment in X value during the course of strain increment is about 137 MPa for LPBF whereas that in cast is close to 370 MPa, with comparable final X values in both cases. LPBF Ni20Cr shows non-linear kinematic hardening, contrary to an almost linear behavior for cast specimen.

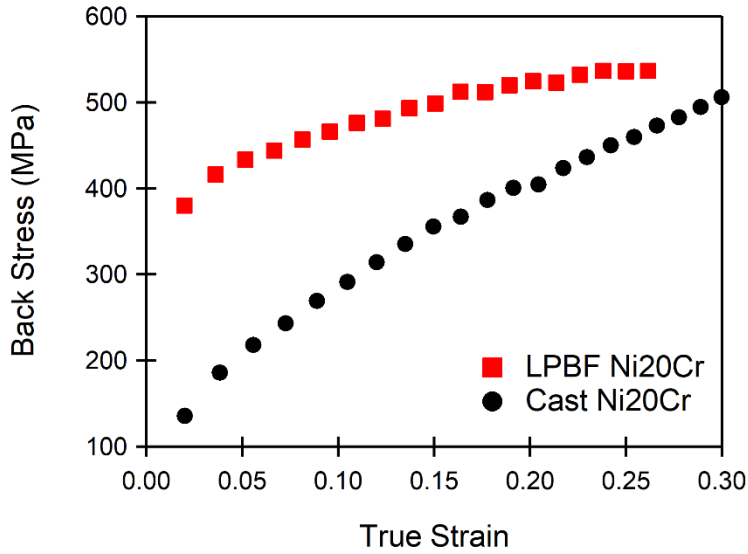


Figure 9: Evolution of the back stress against true strain curve for LPBF and Cast Ni20Cr.

As shown in fig. 10, the effective stress (σ_{eff}) evolution depicts similar slope of increment for both specimens with higher initial value (238 MPa) for LPBF than that of cast (135 MPa).

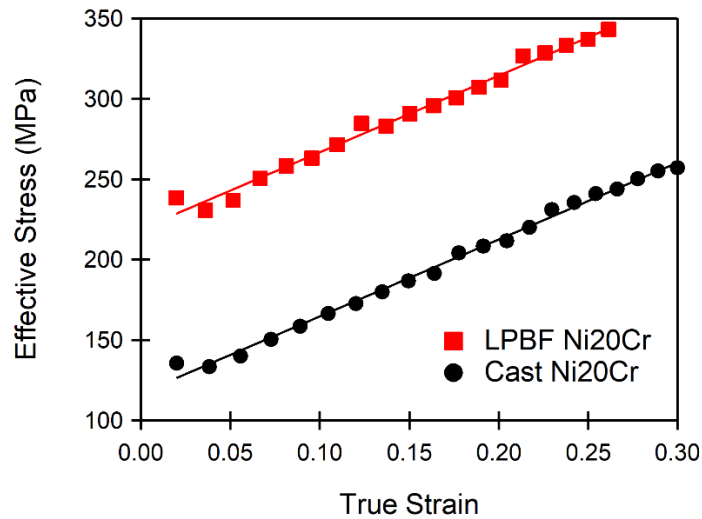


Figure 10: Evolution of the effective stress against true strain curve for LPBF and Cast Ni20Cr.

The further extension of flow stress partition analysis on effective stress enables the estimation of athermal and thermal stresses, as shown in fig. 11(a) and fig. 11(b). Higher athermal stress for LPBF than Cast (close to 100 MPa) is observed but the difference remains the same, independently of the true strain level. Linear isotropic hardening is observed in effective stress curves of both LPBF and cast specimens, as indicated by line fitting as seen in fig. (10). However, when it comes to the thermal partition, cast specimen achieves marginally higher values than that of LPBF (close to 10 MPa in the beginning of plasticity). Nevertheless, the thermally activated part of the effective stress is much lower than the athermal ones revealing the dominant athermal character of local interactions between mobile dislocations and microstructure.

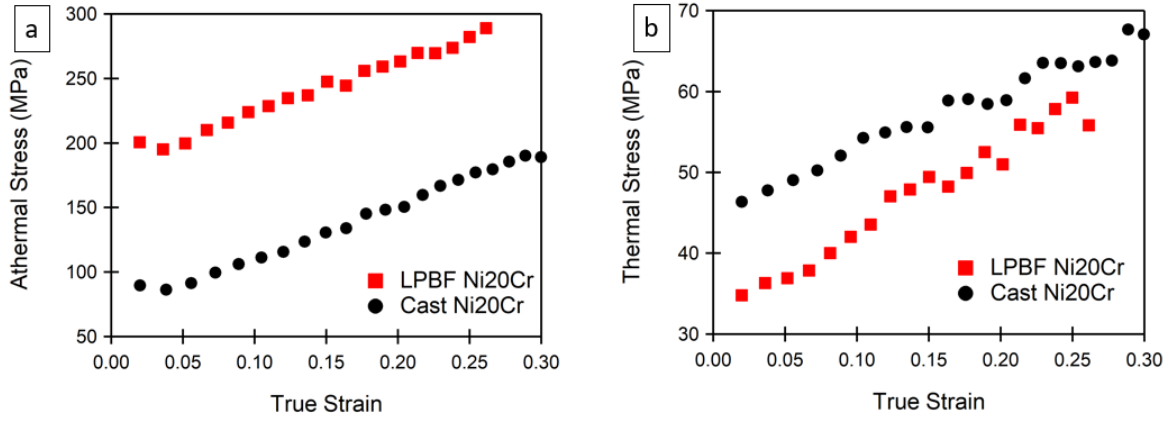


Figure 11: Evolution with true strain of the two components of the effective stress: (a) athermal stress and (b) thermal stress evolution for LPBF and Cast Ni20Cr.

Finally, activation volume is analyzed and compared for the two types of samples. This parameter enables us to characterize the possible contributing mechanism for dislocation mobility (Lilensten et al., 2018; Martin et al., 2002). Physically it can be understood as a volume covered by a dislocation from initial condition to an activated state post deformation (Sarkar and Chakravarty, 2015). Fig. 12 shows the evolution of activation volume against true strain. The initial value for LPBF is about 150 b^3 which shows an initial incremental curve till 0.06 true strain value and then decreases to about 100 b^3 . However, in cast specimen, the value drops from 129 b^3 to 77 b^3 with respect to the true strain, and agree with the Clément et. al. and are much lower than that of pure Ni (1000 b^3) (Clément et al., 1984).

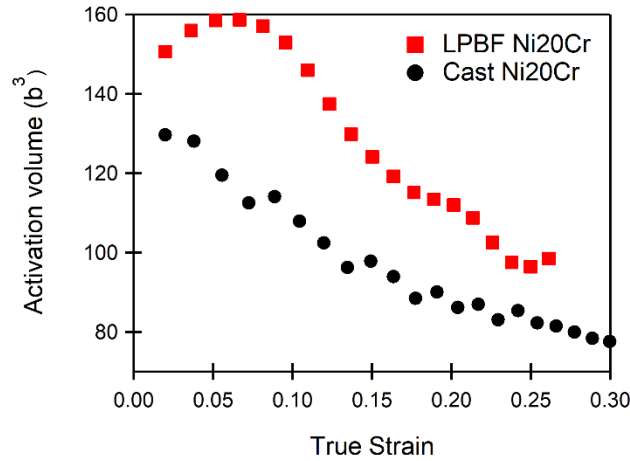


Figure 12: Evolution of the apparent activation volume evolution vs true strain for LPBF and Cast Ni20Cr.

4.4. Deformation microstructures in LPBF and Cast Ni20Cr

Deformation twins, stacking faults (SFs), slip bands are the most common features observed in FCC systems with low stacking fault energy (Cui et al., 2021), which is the case of Ni20Cr (Clément et al., 1984; Hug et al., 2015). In fig. 13(a) and fig. 13(b) related to cast sample deformed close to 0.3 of true strain, dominant distribution of SFs across the micrograph is observed. In all the following micrographs, building direction is in Z-axis and slices of YZ were observed and tensile axis is perpendicular to the building direction and is denoted with an upwards arrow (in the top corner of micrographs). Observations of extended stacking faults

confirms the low stacking fault energy for this material. Most partials are present in the hard zones, as they seem to form at the dislocation walls. Deformation twins were also observed in fig. 13(c) (depicted by red arrows), whereas nano-twins are observed in fig. 13(d), and are highlighted by red circles. The \vec{g} has been marked with yellow arrows.

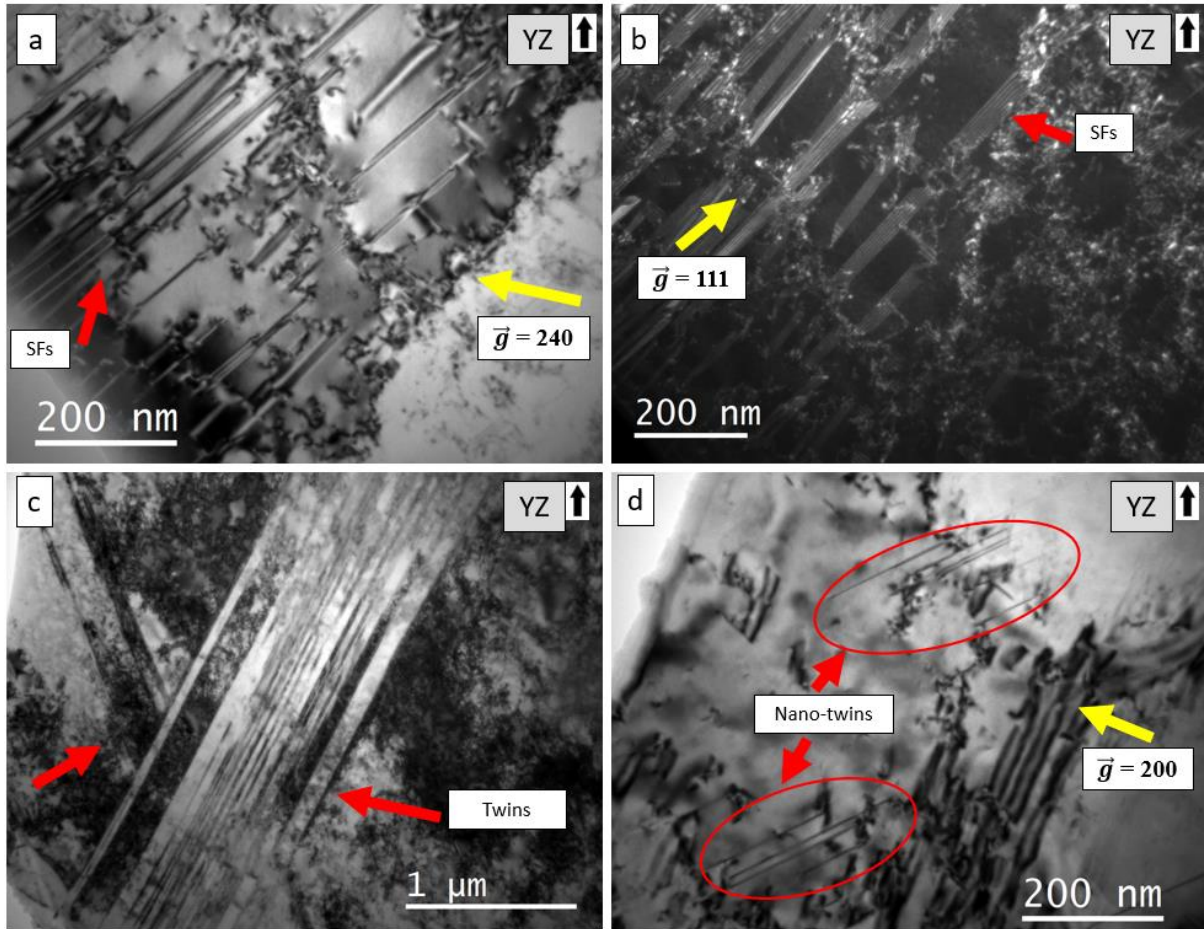


Figure 13: TEM observation of dislocations at 0.3 strain for cast Ni20Cr: (a) stacking faults interacting with dislocations; (b) stacking faults imaged using weak beam TEM technique; (c) deformation twins in bright field condition; and (d) dislocation and second deformation nano-twins observed in bright field mode.

These observed nano-twins were also illustrated in fig. 14(a) and fig. 14(b). Twinned regions have been marked by blue lines and yellow dotted zone is the twin boundary marking a twin in fig. 14(b). Both the zones outside the dotted yellow lines was rendered to diffraction patterns by Fourier transform of respective parts of the image (regions close to blue lines), and the diffraction patterns confirmed the presence of twinned zones. As illustrated at the atomic scale in this former figure, the twin thickness seems to be between 1-2 nm, as already reported in literature (Zhang et al., 2020) corresponding to 3-5 atomic planes.

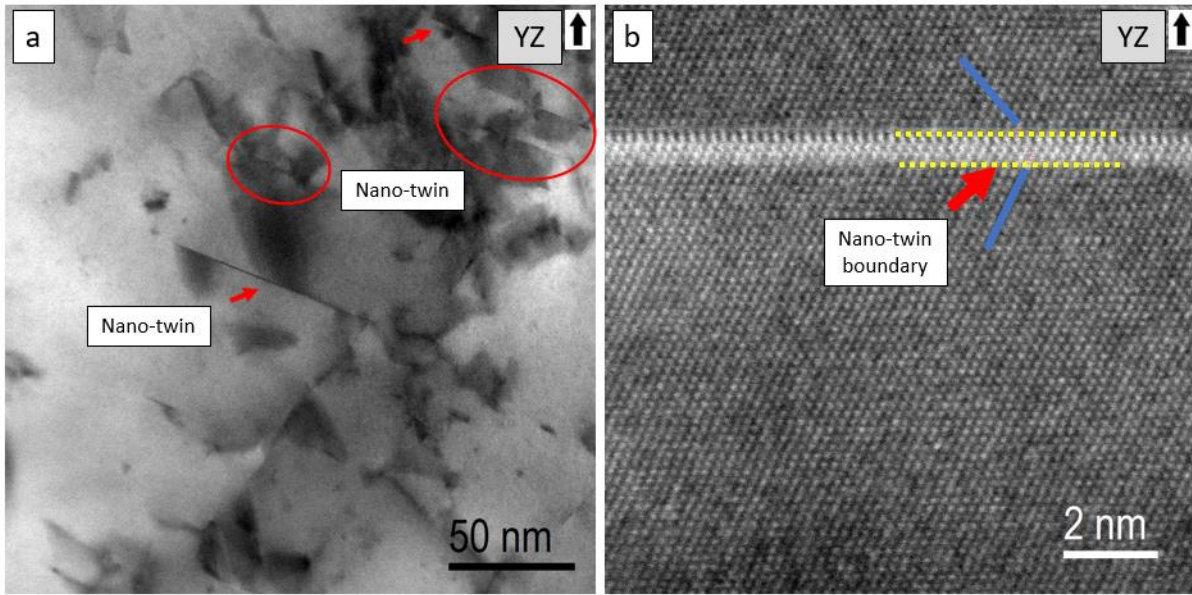


Figure 14: (a) Nano-twins in 30% deformed cast Ni20Cr using bright field BF-STEM; (b) Stacking fault/ nano-twin boundary at atomic scale (BF-HRSTEM).

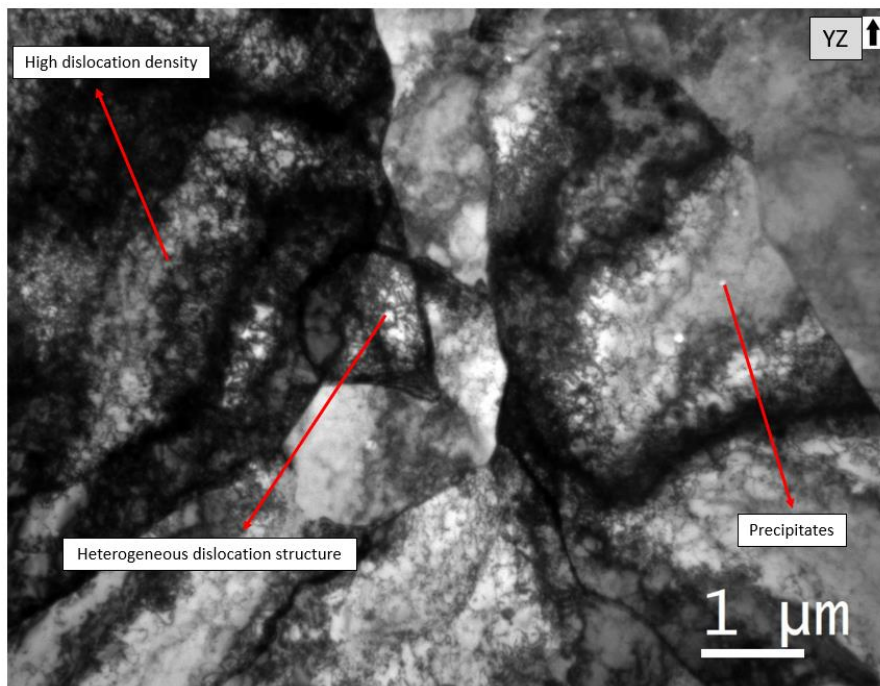


Figure 15: Illustration of the 0.3 deformed microstructure of LPBF specimen using CTEM observed close to a $[110]$ zone axis.

Compared to cast, LPBF specimen subjected to 30% of plastic true strain in tension shows a different dislocation evolution behavior with no occurrence of twinning and no stacking faults related to partial dislocations. This feature is probably due to the enhanced twinning activity due to Short Range Order (SRO) (Park et al., 2010), which is larger for cast than LPBF for this material (Hug et al., 2022; Karmazin et al., 1994). A large dislocation density is observed alongside with cells as seen in fig. 15.

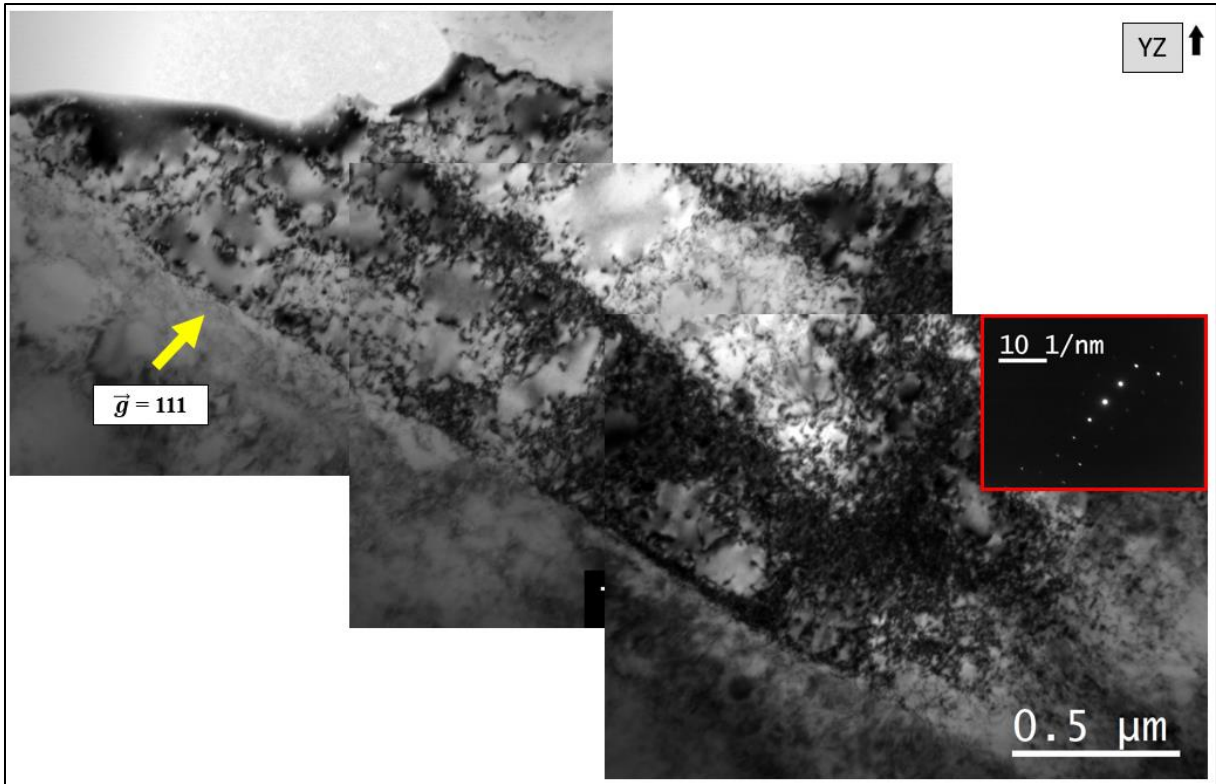


Figure 16: Illustration of dislocation walls associated to dendrites using BF-TEM.

Fig. 16 displays a magnification of cellular walls or hard zones with high dislocation density. Isolated dislocations and dislocation sub-features are observed in the soft zones. Compared to the initial state, dislocation density seems to have been incremented in the wall, increasing, in turn, its width, as seen in fig. 17(a). Fig. 17(b) also illustrates dislocations interacting with precipitates. Dislocations present also interactions with other sub-features as previously seen in fig. 4 (b).

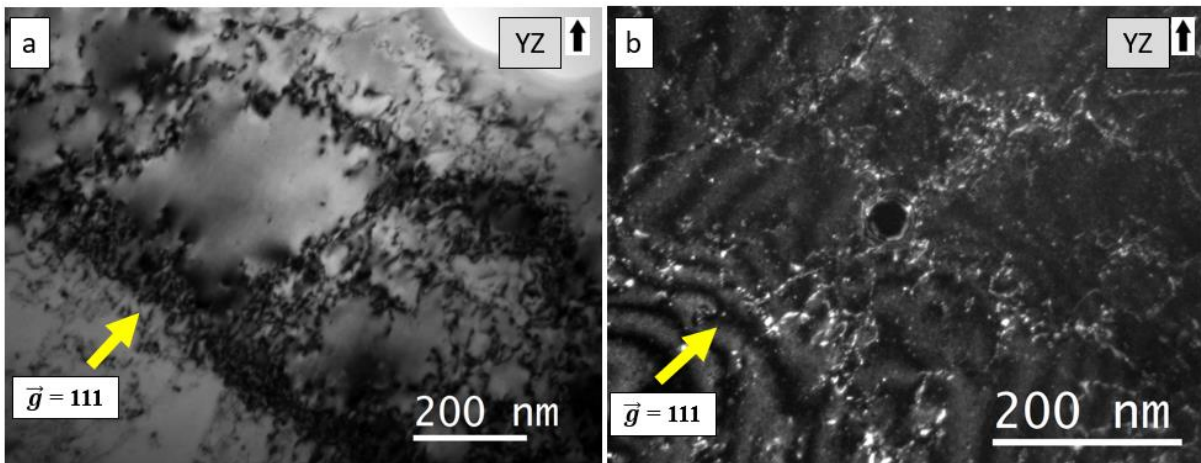


Figure 17: (a) Magnification of cellular dendritic walls using bright field-TEM; (b) illustration of localized interaction between precipitates and dislocations in weak beam-TEM.

4.5. Kocks-Mecking modelling of the tensile behavior

The tensile curves of cast and LPBF samples presented in the section 4.2 were employed to identify the KM model presented in section 3. Based on the microstructure analysis presented in the former paragraphs, eq. 5 related to the derivative of the dislocation density with strain can be simplified. First, bulk specimens are not affected by free surfaces (average distance between free surfaces several orders of magnitude larger than the other microstructure features) and the associated strain hardening term was dismissed for cast and LPBF specimens. Then, for both kind of samples, twinning influence on strain hardening was not considered as only few mechanical twins were evidenced for cast by TEM. Regarding the influence of precipitates on strain hardening, as no precipitation evidence was found for cast, this contribution on eq.5 was not considered. For LPBF samples, Cr-rich precipitates have been characterized inside the dendrite walls. Nevertheless, their influence on strain hardening is supposed to be low as only reduced interaction with mobile dislocations is expected due to the high dislocation density surrounding the precipitates. Consequently, no precipitation contribution to strain hardening was considered for both kind of samples in first approximation. Contrarily to cast exhibiting a full recrystallized character, an initial dislocation structure associated to dendrites was characterized for LPBF samples. Its contribution to strain hardening has been then taken into account for this kind of sample. To sum up, dislocation forest interactions, dislocation annihilation, grain boundaries and initial dislocation structures were considered for strain hardening for LPBF whereas the latter contribution was not considered for cast.

Table 4 summarizes the different parameters of the model alongside to their values resulting from literature identification or microstructure characterization. For Taylor factor a value of 3 has been considered (no texture) whereas 0.3 has been employed for α (average value considering all dislocation interaction (Kocks and Mecking, 2003)). Shear modulus (Calvarin-Amiri et al., 2000) and Burgers vector modulus (Butt and Sattar, 2001) was taken from literature. K_g was considered following the work of Rudloff (Rudloff, n.d.). The grain size d is the average one estimated in this work by Electron Back-Scattered Diffraction analysis for both kind of samples. Based on those values, the optimization process returns the values for β , K_2 and l_0 . Table 5 summarizes the values of these three parameters for each experimental tensile curve considered in this study as well as average values with associated errors (90% of confidence interval). Once identified, the model returns the flow stress and dislocation density evolution with strain.

Table 4: Summary of the values of the different parameters of the Kock-Mecking model identified from literature and microstructure characterization.

	M	α	μ (MPa)	b (mm)	k_g	d (mm)	σ_0 (MPa)
Cast	3	0.3	8.1×10^4	2.5×10^{-7}	5	400	115
LPBF						70	

Table 5: Summary of the values of the different parameters of the Kock-Mecking model identified from modeling of the experimental tensile curves.

Sample type	Test type	Beta (β)	K_2	Dendrite (l_0)
LPBF	LRU attempt 1	2.00E+13	0.838	1.90E-03
	LRU attempt 2	1.00E+10	0.732	2.00E-03
	LRU attempt 3	7.00E+05	0.929	1.70E-03
	LRU attempt 4	4.00E+05	0.889	1.70E-03
	Monotonic attempt 1	2.00E+13	0.963	1.61E-03
	Monotonic attempt 2	1.22E+10	1.24	1.63E-03
	Monotonic attempt 3	3.43E+10	1.17	1.46E-03
	Average	5.72E+12	0.97	1.71E-03
	Error (90 % CI)	6.41E+12	0.13	1.06E-04
Cast	LRU attempt 1	43	1.48	N.A.
	LRU attempt 2	42	1.46	
	Monotonic attempt 1	37	2.06	
	Monotonic attempt 2	44	1.45	
	Monotonic attempt 3	38	2.00	
	Average	40.80	1.69	
	Error (90 % CI)	2.95	0.29	

Fig. 18 illustrates an example of the comparison between one experimental tensile curve and the corresponding predicted one for each manufacturing process. For both LPBF and cast samples, the KM model is able to accurately reproduce the tensile curve. The agreement is better for LPBF than cast, as in the case of cast, the large grain size induces transient behavior (strain hardening stages with inflection point similar to single crystals ones (Keller and Hug, 2017a)).

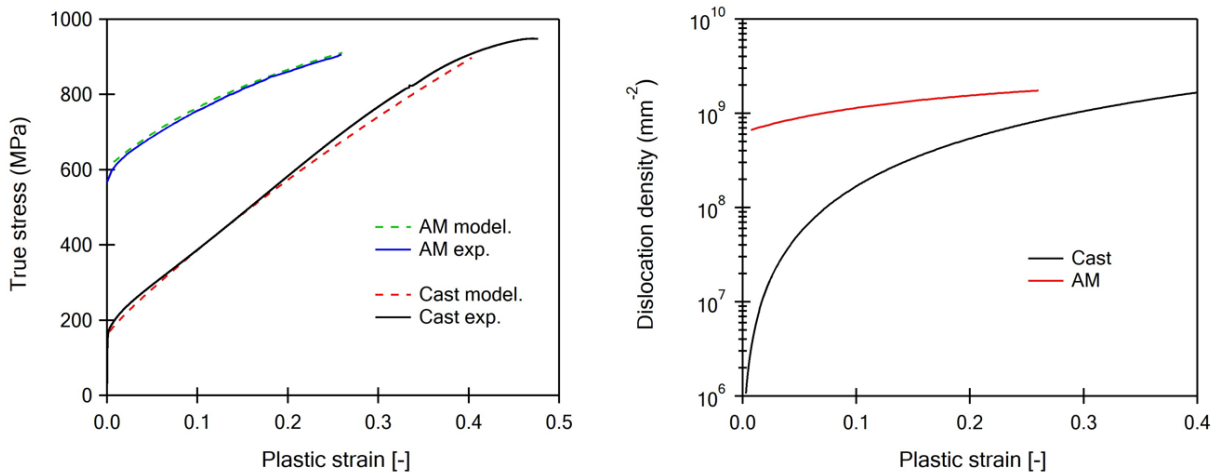


Figure 18: Comparison of the experimental and predicted tensile curves using Kock-Mecking model for LPBF and cast Ni20Cr samples and, (b) comparison of the dislocation density evolution with strain.

The evolution of the dislocation density with strain is displayed in fig. 18(b). The initial value of the dislocation density returned by the KM model for the LPBF sample ($6.2 \times 10^8 \text{ mm}^{-2}$) is about three orders of magnitude higher than the value for cast ($1.5 \times 10^5 \text{ mm}^{-2}$) in agreement with the TEM observations for both samples. For the LPBF sample, the initial value of the dislocation density is close to the one reported in literature for 316L ($6 \times 10^8 \text{ mm}^{-2}$ (Bahl et al., 2019)) and for IN718 ($1.6 \times 10^8 \text{ mm}^{-2}$ (Gallmeyer et al., 2020)). At fracture, the dislocation density is similar for the two samples revealing a larger storage of dislocations in the case of cast compared to LPBF. For stress higher than 600 MPa corresponding to the onset of plasticity for LPBF, cast and LPBF samples do not exhibit the same strain hardening and dislocation density evolution revealing different strain hardening mechanisms. In agreement with their same chemical compositions, the dislocation annihilation rate is similar for the two kinds of sample. Similar KM analysis performed on high purity polycrystalline nickel data from literature (Keller et al., 2011) returns a K_2 value about 3.3. This much lower value for Ni20Cr is in agreement with its planar glide character which restricts the dislocation annihilation events.

5. Discussion

5.1. Initial microstructure for LPBF samples and its influence on the yield stress

The huge difference in all the microstructural features like grain size, dendrites, initial dislocation density, and dislocation substructures has been clearly seen by electron microscopy between LPBF and cast specimens.

At the sub-grain scale, dislocation substructures like stacking fault tetrahedrons (SFTs) and dislocation dipoles as well as dendrites associated to precipitation marks the most important differences between the two kinds of samples. At a larger scale, melting pools found in as-built LPBF specimens can also modify the strain mechanisms for this kind of samples. The formation of SFTs could correspond to a local migration and clustering of vacancies which formed due to intense quenching from high temperatures or from heavy plastic deformation (dislocation reactions and entanglement) (Kojima et al., 1989; Singh et al., 2004). LPBF is known to have extremely high solidification rates of about 10^6 K/s as estimated using the interdendritic arm spacing for Ni20Cr in section 4. Therefore, the presence of these tetrahedrons makes sense even if they have been reported so far mainly for irradiated LPBF manufactured alloys. Their size was found to be around 10 nm, in agreement with literature in conventionally produced materials (Kiritani, 1997) or irradiated IN718 produced by LPBF (Aydogan et al., 2022). Nevertheless, their average spacing is too large to play a role on plasticity. Besides, several studies describe that dislocation loops form when oversaturated vacancies accumulate in a plate form on densely packed lattice planes (Kroupa, 1966; Rühle and Wilkens, 1996). Their observations in fig. 4(b) alongside SFTs seems then to prove that LPBF induces large amount of vacancies.

At the grain level, Electron Back-Scattered Diffraction analysis carried out for LPBF returns a relatively lower value of texture intensity (**2.6**) compared to cast (**7.1**) implying the absence of dominant crystallographic orientations, in agreement with the low manufacturing volumetric energy. Taylor's factors computed for the two materials from EBSD analysis are very similar with value of about **3.1** for LPBF and **3.4** for cast. Those values ensure a similar contribution of grain orientation distribution over the mechanical behavior of the two kinds of samples. The large KAM and GOS values for LBPF compared to cast relates to the high mechanical

quenching inducing misorientation via layer-by-layer high cooling rate assisted manufacturing. Several studies account (Tremisn et al., 2021; Y. Zhao et al., 2021) that such a huge multi-fold difference in GOS values manifests the presence of higher residual stress in LPBF initial state than that of its cast counterpart. In contrast, for cast, an almost defect free microstructure is observed.

High fraction of Low angle grain boundaries (LAGBs) was found in as-built LPBF (around 76% in area) set till 15° misorientation as mentioned in previous section. Kernel average map of LPBF specimens as shown in fig. 5(e) indicates the presence of GNDs close to these LAGBs as discussed in literature for LPBF 316L (Cui et al., 2021), which can be associated to high initial dislocation density observed in as-built of LPBF specimens. High thermal stresses formed due to cyclic tension and compression during the LPBF process need to be accommodated with the help dislocation generation and formation of LAGBs (Cui et al., 2021; Kim et al., 2021).

This multiscale microstructure characterization enables the estimation of each microstructure feature contribution to the yield stress. Using the flow stress partition described in section 3, the yield stress σ^y can be written as a sum of the effective stress and backstress components (intragranular component, X_{intra}^y and intergranular component, X_{inter}^y) at yield point:

$$\sigma^y = \sigma_{eff}^y + X_{intra}^y + X_{inter}^y \quad (7)$$

Considering the different defects characterized in the LPBF samples and assuming that the grain size strengthening is low for this stress component (Wilcox and Clauer, 1972) and can be neglected, the value of the effective stress at the yield point can be also expressed following eq. 8.

$$\sigma_{eff}^y = \sigma_{s.s.} + \sigma_{r.s.d.} \quad (8)$$

where $\sigma_{s.s.}$ represents the solid solution contribution to stress and $\sigma_{r.s.d.}$ the contribution of the regularly spaced defects (r.s.d.) such as isolated dislocations, small precipitates... which is theoretically written as $\sigma_{r.s.d.} = M\mu b/l_d$ with l_d the average defect distance (“Introduction to Dislocations - 5th Edition,” n.d.).

In the case of LPBF Ni20Cr those regularly spaced defects are related to dislocations in the soft zones ρ_s ($l_d = 1/\sqrt{\rho_s}$) and the dendrite walls (separated by the distance l_0). As precipitates are localized inside those walls, their contribution on stress is supposed to be negligible, as already justified in section 4.5. Hence, one could write the initial value of the effective stress such as (Feaugas, 1999; “Introduction to Dislocations - 5th Edition,” n.d.):

$$\sigma_{eff}^y = \sigma_{s.s.} + \alpha M\mu b\sqrt{\rho_s} \quad (9)$$

For Ni20Cr $\sigma_{s.s.}$ can be estimated using the extrapolation of the cast effective stress for zero strain (fig. 10) and is about 115 MPa. This latter is in good agreement with the value reported in literature (Feaugas and Haddou, 2003)(Wilcox and Clauer, 1972) and employed for the KM modelling. TEM images also enable the estimation of the dislocation density in the soft zones. Using the method based on dislocation intercepts with a line network (Fripan and Eckart Exner, 1984; Ham, 1961) applied at five different locations, an average value $\rho_s = (4 \pm 1) \times 10^7 \text{ mm}^{-2}$ was obtained. To compute this dislocation density, an average value of foil thickness of 200 nm has been considered. This value of dislocation density in soft zone is lower than the average

one estimated by the KM modelling (section 4). The value returned by KM model is, indeed, the total dislocation density which take into account the value of this parameter in soft and hard zones. These two values are then consistent.

Using the M , α , μ and b values reported in table 4, the contribution of dislocations on the initial value of the effective stress is about 117 MPa. Solid solution contribution is approximated to be 115 MPa. Hence, at the onset of plasticity, the estimation of the effective stress based on the theoretical contribution of microstructure returns a value of about 232 MPa. This value is in fairly good agreement with the 216 MPa which can be extrapolated from fig. 10 for LPBF samples. Then, the larger value of effective stress for LPBF compared to cast at the onset of plasticity is due to the larger initial dislocation density in soft zone.

When it comes to the backstress, as mentioned in eq. 10, the intergranular component can be expressed using a Hall-Petch formalism, with k_{HP} the slope of the Hall-Petch plot for yield stress. For Ni20Cr, a similar value of about $950 \text{ MPa}\cdot\mu\text{m}^{-1/2}$ was reported for cast (Wilcox and Clauer, 1972) and LPBF (Hug et al., 2022). For the intragranular backstress, following the works of Feaugas (Feaugas, 1999) and Keller et. al. (Keller et al., 2011, 2009) on FCC materials with wavy slip tendency, the intragranular backstress can be expressed as a function of the average hard zones spacing l_0 (see eq. 11). In that case f_g represents the volume fraction of grains presenting such hard zones (here, $f_g=1$ as all grains exhibit cell structures) and K_s a constant depending on the stacking fault energy. For planar glide materials such as Ni20Cr, this relationship is supposed to be also valid (Kuhlmann-Wilsdorf, 1989).

$$X_{inter}^y = \frac{k_{HP}}{\sqrt{d}} \quad (10)$$

$$X_{intra}^y = f_g K_s \frac{\mu b M}{l_0} \quad (11)$$

For LPBF Ni20Cr this average distance l_0 corresponds to the interdendritic arm spacing estimated in section 3. Using k_{HP} value reported in literature for this material, the grain size estimated by Electron Back-Scattered Diffraction, considering in first approximation $K_s=2$ (Feaugas, 1999) (value for 316L with low stacking fault energy) and the M , α , μ and b values reported in table 4, the two backstress components can be estimated: $X_{inter}^y=111$ MPa and $X_{intra}^y=258$ MPa. Those values correspond to a total initial backstress of about 369 MPa in good agreement with the extrapolated value of X about 350 MPa for zero strain in fig. 9 for LPBF samples. The larger backstress value at the onset of plasticity for LPBF compared to cast is due, first, to the reduced grain size for LPBF and, second, to the dendrite walls with a large dislocation density.

Finally, all those contributions to the yield stress enable the estimation of this parameter from a microstructural framework. Those contributions are summarized in table 6. In that case, σ^y is about 601 MPa whereas the value estimated for the tensile curve is 566 MPa. These two values are in very well agreement.

Table 6: Summary of the microstructural contributions (MPa) to the yield stress for LPBF samples.

		Solid solution	Dislocation density in soft zones	Total effective stress	Grain size strengthening	Dendrite long range backstress	Total backstress	Total Yield stress
Micro. framework	absolute value (MPa)	115	117	232	111	258	369	601
	Contribution in %	19.1	19.5	38.6	18.5	42.9	61.4	100
Tensile curve	absolute value (MPa)	N/A	N/A	216	N/A	N/A	350	566

Then table 6 clearly illustrates that about 43% the yield stress for LPBF samples is associated to the presence of dendrites mostly due to the intragranular backstress arising from the differences in dislocation density in the hard zones (dendrite walls) and soft zones. Compared to already reported estimation of dislocation contributions in the yield stress for LPBF alloys considering only the average dislocation density (Bahl et al., 2019), the results obtained for that study clearly show that both absolute value of dislocation density and dislocation distribution into hard (dendrite walls) and soft (dendrite center) zones, are responsible for the enhanced yield stress of LPBF Ni20Cr. Moreover, the grain size contribution to the yield stress is significant but lower than the one related to dendrites, as supposed by other researchers (Bronkhorst et al., 2019). Based on this first modeling attempt, other microstructure contributions to yield stress such as the fraction of LAGBs should be introduced to estimate more accurately the contribution of specific LPBF microstructure features.

5.2. Strain hardening mechanisms

As reported in the former section regarding yield stress, the different microstructural features of LPBF material can play a role on the strain hardening. Nevertheless, contrarily to the yield stress estimation, strain hardening mechanisms can be hardly analyzed using microstructural data. In this case, flow stress, evolution of flow stress components with respect to strain and finally Kocks-Mecking model can be used.

As observed in fig. 7(b), the strain hardening rate for cast specimen shows a constant character (linear relationship between stress and strain) till 30% true strain indicating a very low annihilation of dislocations in agreement with the planar glide character of the material (restricted cross-slip) (Cui et al., 2021; Kuhlmann-Wilsdorf, 1989). Similar analysis done for the LPBF specimens indicates almost non-linear behavior since the beginning of plasticity. As the stacking fault energy is mainly due to the material chemical composition and that this parameter is not very sensitive to slight Cr content variation (Zhang et al., 2020), no difference in cross-slip ability is expected between cast and LPBF samples. The similar K_2 parameter of Kocks-Mecking model confirm this hypothesis (0.97 ± 0.12 for LPBF versus 1.69 ± 0.29 for cast). Contrarily to other papers published in literature for which different values of K_2 have been reported for the same material depending on the manufacturing conditions (Bahl et al., 2019; Jain et al., 2022; X. X. Zhang et al., 2022), the introduction of all the microstructure contributions into eq. 5 returns a similar value of this parameter, in agreement with the similar average chemical composition and same mechanical test temperature. The low dislocation

annihilation by cross-slip cannot be responsible for this difference in strain hardening (linear vs non-linear).

The analysis of the evolution of the effective stress with strain in fig. 10 can provide valuable information about the strain hardening mechanisms in the soft zones. For the effective stress, as mentioned in the former section of the discussion, the grain size strengthening is expected to be low and is then neglected. For the two samples, linear hardening is observed revealing no dislocation annihilation. Hence, in the soft zones, the evolution of the dislocation density with strain can be expressed, in first approximation, by eq. 12 considering only one term related to forest dislocation contribution.

$$\frac{d\rho_s}{d\varepsilon} = \frac{M}{b} \cdot \frac{\sqrt{\rho_s}}{\beta} \quad (12)$$

In the soft zones, following the previous section and eq. 9, the effective stress can be written following eq. 13.

$$\sigma_{eff}(\varepsilon) = \sigma_{s.s.} + \alpha M \mu b \sqrt{\rho_s(\varepsilon)} \quad (13)$$

Considering that the contribution of the solid solution (first term on the right-hand side of eq. 13) does not depend on strain, the strain hardening rate $\frac{d\sigma_{eff}}{d\varepsilon}$ can be formulated as follows (eq. 14):

$$\frac{d\sigma}{d\varepsilon} = \frac{\alpha \mu M^2}{2\beta} = k \quad (14)$$

$$\beta = \frac{\alpha \mu M^2}{2k} \quad (15)$$

Using fig. 10, k , which is the strain hardening rate, is estimated to 498 ± 8 MPa and 487 ± 18 MPa for cast and LPBF samples respectively. Using those values and eq. 15, similar values of β of about 219 ± 4 and 224 ± 8 for cast and LPBF samples in the order given. These two values, corresponding to the ratio between the dislocation mean free path and average dislocation distance, illustrates that same dislocation production based on the forest interactions could be responsible of the strain hardening in the soft zones. The SFTs, dipoles and loops observed in the LPBF compared to cast seem, hence, not to affect the dislocation production at this scale.

The initial dislocation mean free path L_0 can be estimated using β and the average dislocation density in the soft zones: $L_0 = \beta / \sqrt{\rho_s}$. For cast, no experimental measurements of the initial dislocation density have been done. Nevertheless, considering the initial value computed by the KM model in fig. 18(b), the initial value of the dislocation mean free path for the cast material is about $570 \mu\text{m}$, in the same order of magnitude than the grain size, in agreement with the almost defect free microstructure for that material.

For LPBF samples, considering the ρ_s experimental value reported in the previous section for the as-built state, L_0 is about $13 \mu\text{m}$. Nevertheless, this value is more than one order of magnitude larger than the dendritic primary arm spacing which must restrict the dislocation glide. Considering that dendrite grows following the $\{001\}$ direction for f.c.c. metals, slip directions (i.e. $\{110\}$ directions) with respect to the dendrite walls are inclined by either 90° or 45° . The maximal average distance between two dendrites walls alongside the dislocation slip direction is then of about $0.7 \mu\text{m}$. This value is far lower than the L_0 value obtained here. Hence,

another dislocation production mechanism can be also operating for LPBF samples in the soft zones.

To better analyze the microstructure contribution to dislocation production, the general Kocks-Mecking formalism applied to the flow stress (described in sections 3 and 4.5) can be employed. Once the model identified on experimental tensile curves (see fig. 18), the estimation of each microstructure contribution to dislocation evolution with strain can be obtained. For cast, as explained in section 4.5, the derivative of the dislocation with plastic strain can be written following eq. 16 whereas the one for LPBF can be expressed by eq. 17.

$$\frac{d\rho}{d\varepsilon_p}^{cast} = \frac{M\sqrt{\rho}}{\beta b} + \frac{Mk_g}{bd} - K_2\rho \quad (16)$$

$$\frac{d\rho}{d\varepsilon_p}^{AM} = \frac{M\sqrt{\rho}}{\beta b} + \frac{Mk_g}{bd} - K_2\rho + \frac{M}{bl_0} \quad (17)$$

Using the KM model parameters identified in section 4.5 (table 4 and table 5), it is possible to compute the value of each terms of eq. 16 and eq. 17 (for cast and LPBF samples, respectively) as a function of strain. Fig. 19 illustrates the positive contributions to dislocation production for the two samples.

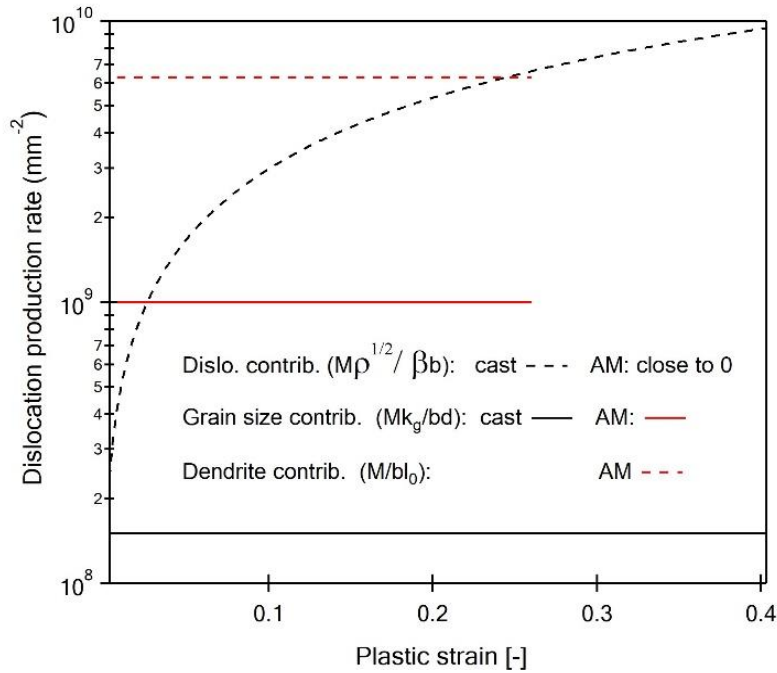


Figure 19: Evolution of the different microstructure feature contributions to the dislocation production rate estimated by the Kocks-Mecking model.

For cast, following eq. 16, only two terms associated to forest dislocation interaction and grain size participate to the dislocation production with strain. For that material, the grain size contribution is lower than the forest dislocation terms due to the large grain size for this sample (400 μm). The average β value associated to the KM model for cast is about 46 (see table 5) which is lower than the value computed for effective stress only and in good agreement with values reported for this material (Mecking, 1975).

For LPBF, β tends to infinity meaning that the dislocation production based on forest interaction is neglectable compared to other dislocation production mechanisms. In that case, the

dislocation production rate is dominated by the term related to the initial dislocation structures and, considering the model formulation, this can be only achieved by an infinite value of β (which, in that case, does not correspond to a physical value). This result is in agreement with the experimental work of Bean and co-workers (Bean et al., 2022) who identified dendrites as source mechanisms for strain hardening for 316L. The identification of the l_0 value using KM model returns a value of about 2 μm which is four times the value characterized experimentally (see table 4). The non-linear strain hardening for LPBF samples is then due to the dislocation production related to dendrites. The larger predicted value of the dendrite size based on the Kocks-Mecking model could be due to the fact that dendrite walls can be crossed by dislocations. This feature is in agreement with the five times larger dislocation mean free path prediction using crystalline plasticity models and dislocation cells measurements for pure nickel (Keller and Hug, 2017b). Considering the flow stress components evolution with strain, this dendrite dislocation production must affect the backstress and, in particular, the dislocation density in the hard zones, as observed in TEM analysis fig. 16 and fig. 17(a) compared to fig. 3(b). Nevertheless, it could also increase the dislocation density in the soft zone, explaining the poor agreement between dislocation mean free path and dendrite size when only forest dislocation production mechanisms are considered in the soft zones.

When it comes to finite element modelling of LPBF mechanical behavior using crystalline plasticity constitutive laws, results obtained in these two sections proved that the microstructural length associated to dendrites has to be considered both for stress and strain hardening for an accurate and physical modelling.

6. Conclusions

Using a Ni20Cr alloy with a simplified microstructure and planar glide tendency, this work has point out a clear distinction in mechanical behavior brought about by process change i.e. Laser Powder Bed Fusion process with respect to that of conventional manufacturing techniques. Using tensile tests, dislocation analysis and Kocks-Mecking formalism, the relationship between the basic microstructural features and the flow stress as well as the strain hardening have been clarified for additive manufacturing alloys. The main conclusions of this work are listed as follows:

- The large cooling rates involved by the laser powder bed fusion process induce various dislocation features like dipoles and stacking fault tetrahedra.
- The enhanced yield stress of as-built LPBF samples compared to cast is due to both increments in the effective stress and backstress.
- The effective stress is higher for LPBF compared to cast due to the increase in dislocation density in soft zones but also the presence of solid solution hardening. The difference in dislocation density between soft zones and dendrite walls is responsible for the strong increase in backstress for samples processed by LPBF. Close to 43% of the yield stress for LPBF is related to the presence of solidification dendrites.

- No dislocation production based on forest interaction seems to be operating for LPBF samples and strain hardening is mostly related to dislocation production linked to the dendrites. Consequently, despite pronounced planar glide, Ni20Cr samples produced by LPBF do not prompt any linear strain hardening.
- LPBF Ni20Cr shows higher activation volume than Cast Ni20Cr due to enhanced Short Range Order in cast which could also promotes mechanical twinning compared to LPBF.

Acknowledgements

The Labex EMC3 is greatly acknowledged for the financial support of the Nichrofab project.

References

- Acar, S.S., Bulut, O., Yalçinkaya, T., 2022. Crystal plasticity modeling of additively manufactured metallic microstructures. *Procedia Structural Integrity*, 2nd International Workshop on Plasticity, Damage and Fracture of Engineering Materials (IWPDF 2021), 18-20 August 2021, Ankara, Turkey. 35, 219–227. <https://doi.org/10.1016/j.prostr.2021.12.068>
- Ashby, M.F., 1970. The deformation of plastically non-homogeneous materials. *The Philosophical Magazine: A Journal of Theoretical Experimental and Applied Physics* 21, 399–424. <https://doi.org/10.1080/14786437008238426>
- Aydogan, E., El-Atwani, O., Erdem, B., Chen, W.-Y., Li, M., Devaraj, A., Koc, B., Maloy, S.A., 2022. In-situ radiation response of additively manufactured modified Inconel 718 alloys. *Additive Manufacturing* 51, 102601. <https://doi.org/10.1016/j.addma.2022.102601>
- Bahl, S., Mishra, S., Yazar, K.U., Kola, I.R., Chatterjee, K., Suwas, S., 2019. Non-equilibrium microstructure, crystallographic texture and morphological texture synergistically result in unusual mechanical properties of 3D printed 316L stainless steel. *Additive Manufacturing* 28, 65–77. <https://doi.org/10.1016/j.addma.2019.04.016>
- Bambach, M., Sizova, I., Szyndler, J., Bennett, J., Hyatt, G., Cao, J., Papke, T., Merklein, M., 2021. On the hot deformation behavior of Ti-6Al-4V made by additive manufacturing. *Journal of Materials Processing Technology* 288, 116840. <https://doi.org/10.1016/j.jmatprotec.2020.116840>
- Bean, C., Wang, F., Charpagne, M.A., Villechaise, P., Valle, V., Agnew, S.R., Gianola, D.S., Pollock, T.M., Stinville, J.C., 2022. Heterogeneous slip localization in an additively manufactured 316L stainless steel. *International Journal of Plasticity* 159, 103436. <https://doi.org/10.1016/j.ijplas.2022.103436>
- Beese, A.M., Wang, Z., Stoica, A.D., Ma, D., 2018. Absence of dynamic strain aging in an additively manufactured nickel-base superalloy. *Nat Commun* 9, 2083. <https://doi.org/10.1038/s41467-018-04473-5>
- Blakey-Milner, B., Gradl, P., Snedden, G., Brooks, M., Pitot, J., Lopez, E., Leary, M., Berto, F., du Plessis, A., 2021. Metal additive manufacturing in aerospace: A review. *Materials & Design* 209, 110008. <https://doi.org/10.1016/j.matdes.2021.110008>
- Bronkhorst, C.A., Mayeur, J.R., Livescu, V., Pokharel, R., Brown, D.W., Gray, G.T., 2019. Structural representation of additively manufactured 316L austenitic stainless steel. *International Journal of Plasticity* 118, 70–86. <https://doi.org/10.1016/j.ijplas.2019.01.012>
- Butt, M.Z., Sattar, U., 2001. Deformation behavior of nickel-chromium alloys with special reference to the nature of solute distribution. *Journal of Materials Science Letters* 20, 759–761. <https://doi.org/10.1023/A:1010991816598>

- Calvarin-Amiri, G., Molins, R., Huntz, A.M., 2000. Effect of the Application of a Mechanical Load on the Oxide-Layer Microstructure and on the Oxidation Mechanism of Ni–20Cr Foils. *Oxidation of Metals* 53, 399–426. <https://doi.org/10.1023/A:1004553623556>
- Clément, N., Caillard, D., Martin, J.L., 1984. Heterogeneous deformation of concentrated Ni–Cr F.C.C. alloys: Macroscopic and microscopic behaviour. *Acta Metallurgica* 32, 961–975. [https://doi.org/10.1016/0001-6160\(84\)90034-8](https://doi.org/10.1016/0001-6160(84)90034-8)
- Cui, L., Jiang, F., Deng, D., Xin, T., Sun, X., Mousavian, R.T., Peng, R.L., Yang, Z., Moverare, J., 2021. Cyclic response of additive manufactured 316L stainless steel: The role of cell structures. *Scripta Materialia* 205, 114190. <https://doi.org/10.1016/j.scriptamat.2021.114190>
- Das, S., Seol, J.B., Kim, Y.C., Park, C.G., 2010. Structure and mechanical properties of Ni–Cr alloy produced by single roll strip casting. *Materials & Design* 31, 570–573. <https://doi.org/10.1016/j.matdes.2009.07.006>
- DebRoy, T., Wei, H.L., Zuback, J.S., Mukherjee, T., Elmer, J.W., Milewski, J.O., Beese, A.M., Wilson-Heid, A., De, A., Zhang, W., 2018. Additive manufacturing of metallic components – Process, structure and properties. *Progress in Materials Science* 92, 112–224. <https://doi.org/10.1016/j.pmatsci.2017.10.001>
- Dehoff, R.R., Kirka, M.M., List, F.A., Unocic, K.A., Sames, W.J., 2015. Crystallographic texture engineering through novel melt strategies via electron beam melting: Inconel 718. *Materials Science and Technology* 31, 939–944. <https://doi.org/10.1179/1743284714Y.0000000697>
- Dickson, J.I., Boutin, J., Handfield, L., 1984. A comparison of two simple methods for measuring cyclic internal and effective stresses. *Materials Science and Engineering* 64, L7–L11. [https://doi.org/10.1016/0025-5416\(84\)90083-1](https://doi.org/10.1016/0025-5416(84)90083-1)
- Doquet, V., 1993. Twinning and multiaxial cyclic plasticity of a low stacking-fault-energy f.c.c. alloy. *Acta Metallurgica et Materialia* 41, 2451–2459. [https://doi.org/10.1016/0956-7151\(93\)90325-M](https://doi.org/10.1016/0956-7151(93)90325-M)
- Essmann, U., Mughrabi, H., 1979. Annihilation of dislocations during tensile and cyclic deformation and limits of dislocation densities. *Philosophical Magazine A* 40, 731–756. <https://doi.org/10.1080/01418617908234871>
- Essmann, U., Rapp, M., Wilkens, M., 1968. Die versetzungsanordnung in plastisch verformten kupfer-vielkristallen. *Acta Metallurgica* 16, 1275–1287. [https://doi.org/10.1016/0001-6160\(68\)90008-4](https://doi.org/10.1016/0001-6160(68)90008-4)
- Fan, X., Tang, Q., Feng, Q., Ma, S., Song, J., Jin, M., Guo, F., Jin, P., 2021. Design, mechanical properties and energy absorption capability of graded-thickness triply periodic minimal surface structures fabricated by selective laser melting. *International Journal of Mechanical Sciences* 204, 106586. <https://doi.org/10.1016/j.ijmecsci.2021.106586>
- Feaugas, X., 1999. On the origin of the tensile flow stress in the stainless steel AISI 316L at 300 K: back stress and effective stress. *Acta Materialia* 47, 3617–3632. [https://doi.org/10.1016/S1359-6454\(99\)00222-0](https://doi.org/10.1016/S1359-6454(99)00222-0)
- Feaugas, X., Haddou, H., 2003. Grain-size effects on tensile behavior of nickel and AISI 316L stainless steel. *Metall Mater Trans A* 34, 2329–2340. <https://doi.org/10.1007/s11661-003-0296-5>
- Field, D.P., Bradford, L.T., Nowell, M.M., Lillo, T.M., 2007. The role of annealing twins during recrystallization of Cu. *Acta Materialia* 55, 4233–4241. <https://doi.org/10.1016/j.actamat.2007.03.021>
- Fripan, M., Eckart Exner, H., 1984. Three-Dimensional orientation and roughness of surfaces. *Acta Stereol* 181–186.
- Gallmeyer, T.G., Moorthy, S., Kappes, B.B., Mills, M.J., Amin-Ahmadi, B., Stebner, A.P., 2020. Knowledge of process-structure-property relationships to engineer better heat treatments for laser powder bed fusion additive manufactured Inconel 718. *Additive Manufacturing* 31, 100977. <https://doi.org/10.1016/j.addma.2019.100977>
- Ghorbanpour, S., Alam, M.E., Ferreri, N.C., Kumar, A., McWilliams, B.A., Vogel, S.C., Bicknell, J., Beyerlein, I.J., Knezevic, M., 2020. Experimental characterization and crystal plasticity modeling of anisotropy, tension-compression asymmetry, and texture evolution of additively

- manufactured Inconel 718 at room and elevated temperatures. *International Journal of Plasticity* 125, 63–79. <https://doi.org/10.1016/j.ijplas.2019.09.002>
- Gil Sevillano, J., 1993. The Cold Worked State. *MSF* 113–115, 19–28. <https://doi.org/10.4028/www.scientific.net/MSF.113-115.19>
- Gokcekaya, O., Ishimoto, T., Hibino, S., Yasutomi, J., Narushima, T., Nakano, T., 2021. Unique crystallographic texture formation in Inconel 718 by laser powder bed fusion and its effect on mechanical anisotropy. *Acta Materialia* 212, 116876. <https://doi.org/10.1016/j.actamat.2021.116876>
- Gorse, S., Hutchinson, C., Gouné, M., Banerjee, R., 2017. Additive manufacturing of metals: a brief review of the characteristic microstructures and properties of steels, Ti-6Al-4V and high-entropy alloys. *Science and Technology of Advanced Materials* 18, 584–610. <https://doi.org/10.1080/14686996.2017.1361305>
- Hagihara, K., Nakano, T., 2022. Control of Anisotropic Crystallographic Texture in Powder Bed Fusion Additive Manufacturing of Metals and Ceramics—A Review. *JOM* 74, 1760–1773. <https://doi.org/10.1007/s11837-021-04966-7>
- Ham, R.K., 1961. The determination of dislocation densities in thin films. *The Philosophical Magazine: A Journal of Theoretical Experimental and Applied Physics* 6, 1183–1184. <https://doi.org/10.1080/14786436108239679>
- Herzog, D., Seyda, V., Wycisk, E., Emmelmann, C., 2016. Additive manufacturing of metals. *Acta Materialia* 117, 371–392. <https://doi.org/10.1016/j.actamat.2016.07.019>
- Hug, E., Dubos, P.A., Keller, C., Duchêne, L., Habraken, A.M., 2015. Size effects and temperature dependence on strain-hardening mechanisms in some face centered cubic materials. *Mechanics of Materials* 91, 136–151. <https://doi.org/10.1016/j.mechmat.2015.07.001>
- Hug, E., Lelièvre, M., Folton, C., Ribet, A., Martinez-Celis, M., Keller, C., 2022. Additive manufacturing of a Ni-20 wt%Cr binary alloy by laser powder bed fusion: Impact of the microstructure on the mechanical properties. *Materials Science and Engineering: A* 834, 142625. <https://doi.org/10.1016/j.msea.2022.142625>
- Introduction to Dislocations - 5th Edition [WWW Document], n.d. URL <https://www.elsevier.com/books/introduction-to-dislocations/hull/978-0-08-096672-4> (accessed 6.10.22).
- Jain, R., Yadava, M., Nayan, N., Gurao, N.P., 2022. Combinatorial synchrotron diffraction-constitutive modelling-crystal plasticity simulation framework for direct metal laser sintered AlSi10Mg alloy. *Materialia* 22, 101395. <https://doi.org/10.1016/j.mtla.2022.101395>
- Karmazin, L., Krejčí, J., Zeman, J., 1994. γ Phase and Ni₂Cr-type long-range order in Ni-rich NiCrMo alloys. *Materials Science and Engineering: A* 183, 103–109. [https://doi.org/10.1016/0921-5093\(94\)90894-X](https://doi.org/10.1016/0921-5093(94)90894-X)
- Keller, C., Hug, E., 2017a. Kocks-Mecking analysis of the size effects on the mechanical behavior of nickel polycrystals. *International Journal of Plasticity* 98, 106–122. <https://doi.org/10.1016/j.ijplas.2017.07.003>
- Keller, C., Hug, E., 2017b. Kocks-Mecking analysis of the size effects on the mechanical behavior of nickel polycrystals. *International Journal of Plasticity* 98, 106–122. <https://doi.org/10.1016/j.ijplas.2017.07.003>
- Keller, C., Hug, E., Chateigner, D., 2009. On the origin of the stress decrease for nickel polycrystals with few grains across the thickness. *Materials Science and Engineering: A* 500, 207–215. <https://doi.org/10.1016/j.msea.2008.09.054>
- Keller, C., Hug, E., Feaugas, X., 2011. Microstructural size effects on mechanical properties of high purity nickel. *International Journal of Plasticity* 27, 635–654. <https://doi.org/10.1016/j.ijplas.2010.08.002>
- Keller, C., Margulies, M.M., Hadjem-Hamouche, Z., Guillot, I., 2010. Influence of the temperature on the tensile behaviour of a modified 9Cr–1Mo T91 martensitic steel. *Materials Science and Engineering: A* 527, 6758–6764. <https://doi.org/10.1016/j.msea.2010.07.021>

- Keller, C., Mokhtari, M., Vieille, B., Briatta, H., Bernard, P., 2021. Influence of a rescanning strategy with different laser powers on the microstructure and mechanical properties of Hastelloy X elaborated by powder bed fusion. *Materials Science and Engineering: A* 803, 140474. <https://doi.org/10.1016/j.msea.2020.140474>
- Kelly, C.N., Kahra, C., Maier, H.J., Gall, K., 2021. Processing, structure, and properties of additively manufactured titanium scaffolds with gyroid-sheet architecture. *Additive Manufacturing* 41, 101916. <https://doi.org/10.1016/j.addma.2021.101916>
- Kim, Y.-K., Baek, M.-S., Yang, S., Lee, K.-A., 2021. In-situ formed oxide enables extraordinary high-cycle fatigue resistance in additively manufactured CoCrFeMnNi high-entropy alloy. *Additive Manufacturing* 38, 101832. <https://doi.org/10.1016/j.addma.2020.101832>
- Kiritani, M., 1997. Story of stacking fault tetrahedra. *Materials Chemistry and Physics* 50, 133–138. [https://doi.org/10.1016/S0254-0584\(97\)80250-7](https://doi.org/10.1016/S0254-0584(97)80250-7)
- Kocks, U.F., Mecking, H., 2003. Physics and phenomenology of strain hardening: the FCC case. *Progress in Materials Science* 48, 171–273. [https://doi.org/10.1016/S0079-6425\(02\)00003-8](https://doi.org/10.1016/S0079-6425(02)00003-8)
- Kojima, S., Satoh, Y., Taoka, H., Ishida, I., Yoshiie, T., Kiritani, M., 1989. Confirmation of vacancy-type stacking fault tetrahedra in quenched, deformed and irradiated face-centred cubic metals. *Philosophical Magazine A* 59, 519–532. <https://doi.org/10.1080/01418618908229782>
- Krakhmalev, P., Fredriksson, G., Svensson, K., Yadroitsev, I., Yadroitsava, I., Thuvander, M., Peng, R., 2018. Microstructure, Solidification Texture, and Thermal Stability of 316 L Stainless Steel Manufactured by Laser Powder Bed Fusion. *Metals* 8, 643. <https://doi.org/10.3390/met8080643>
- Kroupa, F., 1966. DISLOCATION DIPOLES AND DISLOCATION LOOPS. *Journal de Physique Colloques* 27, C3-154-C3-167. <https://doi.org/10.1051/jphyscol:1966320>
- Kubin, L., Hoc, T., Devincere, B., 2009. Dynamic recovery and its orientation dependence in face-centered cubic crystals. *Acta Materialia* 57, 2567–2575. <https://doi.org/10.1016/j.actamat.2009.02.013>
- Kuhlmann-Wilsdorf, D., 1989. Theory of plastic deformation: - properties of low energy dislocation structures. *Materials Science and Engineering: A* 113, 1–41. [https://doi.org/10.1016/0921-5093\(89\)90290-6](https://doi.org/10.1016/0921-5093(89)90290-6)
- Lilensten, L., Couzinié, J.-P., Perrière, L., Hocini, A., Keller, C., Dirras, G., Guillot, I., 2018. Study of a bcc multi-principal element alloy: Tensile and simple shear properties and underlying deformation mechanisms. *Acta Materialia* 142, 131–141. <https://doi.org/10.1016/j.actamat.2017.09.062>
- Liu, L., Ding, Q., Zhong, Y., Zou, J., Wu, J., Chiu, Y.-L., Li, J., Zhang, Z., Yu, Q., Shen, Z., 2018. Dislocation Network in Additive Manufactured Steel Breaks Strength–Ductility Trade-Off. *Materials Today* 21, 354–361. <https://doi.org/10.1016/j.mattod.2017.11.004>
- Marnier, G., Keller, C., Taleb, L., 2016. Tensile prestrain memory effect on subsequent cyclic behavior of FCC metallic materials presenting different dislocations slip modes. *International Journal of Plasticity* 78, 64–83. <https://doi.org/10.1016/j.ijplas.2015.11.001>
- Martin, J.L., Lo Piccolo, B., Kruml, T., Bonneville, J., 2002. Characterization of thermally activated dislocation mechanisms using transient tests. *Materials Science and Engineering: A* 322, 118–125. [https://doi.org/10.1016/S0921-5093\(01\)01124-8](https://doi.org/10.1016/S0921-5093(01)01124-8)
- Mecking, H., 1975. Description of hardening curves of fcc single- and polycrystals (No. CONF-751164-3). Argonne National Lab., Ill. (USA).
- Mecking, H., Kocks, U.F., 1981. Kinetics of flow and strain-hardening. *Acta Metallurgica* 29, 1865–1875. [https://doi.org/10.1016/0001-6160\(81\)90112-7](https://doi.org/10.1016/0001-6160(81)90112-7)
- Mecking, H., Kocks, U.F., Fischer, H., 1976. Hardening, recovery, and creep in fcc mono- and polycrystals, Presented at the 4th Intern. Conf. on Strength of Metals and Alloys.
- Mughrabi, H., 1983. Dislocation wall and cell structures and long-range internal stresses in deformed metal crystals. *Acta Metallurgica* 31, 1367–1379. [https://doi.org/10.1016/0001-6160\(83\)90007-X](https://doi.org/10.1016/0001-6160(83)90007-X)

- Mukherjee, M., 2019. Effect of build geometry and orientation on microstructure and properties of additively manufactured 316L stainless steel by laser metal deposition. *Materialia* 7, 100359. <https://doi.org/10.1016/j.mtla.2019.100359>
- Nadammal, N., Mishurova, T., Fritsch, T., Serrano-Munoz, I., Kromm, A., Haberland, C., Portella, P.D., Bruno, G., 2021. Critical role of scan strategies on the development of microstructure, texture, and residual stresses during laser powder bed fusion additive manufacturing. *Additive Manufacturing* 38, 101792. <https://doi.org/10.1016/j.addma.2020.101792>
- Narutani, T., Takamura, J., 1991. Grain-size strengthening in terms of dislocation density measured by resistivity. *Acta Metallurgica et Materialia* 39, 2037–2049. [https://doi.org/10.1016/0956-7151\(91\)90173-X](https://doi.org/10.1016/0956-7151(91)90173-X)
- Nezhadfar, P.D., Thompson, S., Saharan, A., Phan, N., Shamsaei, N., 2021. Structural integrity of additively manufactured aluminum alloys: Effects of build orientation on microstructure, porosity, and fatigue behavior. *Additive Manufacturing* 47, 102292. <https://doi.org/10.1016/j.addma.2021.102292>
- Pantazopoulos, G., 2019. A Short Review on Fracture Mechanisms of Mechanical Components Operated under Industrial Process Conditions: Fractographic Analysis and Selected Prevention Strategies. *Metals* 9, 148. <https://doi.org/10.3390/met9020148>
- Park, K.-T., Jin, K.G., Han, S.H., Hwang, S.W., Choi, K., Lee, C.S., 2010. Stacking fault energy and plastic deformation of fully austenitic high manganese steels: Effect of Al addition. *Materials Science and Engineering: A* 527, 3651–3661. <https://doi.org/10.1016/j.msea.2010.02.058>
- Polák, J., Fardoun, F., Degallaix, S., 1996. Effective and internal stresses in cyclic straining of 316 stainless steel. *Materials Science and Engineering: A* 215, 104–112. [https://doi.org/10.1016/0921-5093\(96\)10373-7](https://doi.org/10.1016/0921-5093(96)10373-7)
- Rudloff, M., n.d. Etude des mécanismes de transition volume/surface du comportement mécanique d'un alliage Ni20Cr 200.
- Rühle, M., Wilkens, M., 1996. CHAPTER 11 - TRANSMISSION ELECTRON MICROSCOPY, in: Cahn, R.W., Haasen†, P. (Eds.), *Physical Metallurgy (Fourth Edition)*. North-Holland, Oxford, pp. 1033–1113. <https://doi.org/10.1016/B978-044489875-3/50016-8>
- Sarantopoulos, D.M., Beck, K.A., Holsen, R., Berzins, D.W., 2011. Corrosion of CoCr and NiCr dental alloys alloyed with palladium. *The Journal of Prosthetic Dentistry* 105, 35–43. [https://doi.org/10.1016/S0022-3913\(10\)60188-6](https://doi.org/10.1016/S0022-3913(10)60188-6)
- Sarkar, A., Chakravarty, J.K., 2015. Activation Volume and Density of Mobile Dislocations in Plastically Deforming Zr-1pctSn-1pctNb-0.1pctFe Alloy. *Metall Mater Trans A* 46, 5638–5643. <https://doi.org/10.1007/s11661-015-3153-4>
- Shifeng, W., Shuai, L., Qingsong, W., Yan, C., Sheng, Z., Yusheng, S., 2014. Effect of molten pool boundaries on the mechanical properties of selective laser melting parts. *Journal of Materials Processing Technology* 214, 2660–2667. <https://doi.org/10.1016/j.jmatprotec.2014.06.002>
- Singh, B.N., Golubov, S.I., Trinkaus, H., Edwards, D.J., Eldrup, M., 2004. Review: Evolution of stacking fault tetrahedra and its role in defect accumulation under cascade damage conditions. *Journal of Nuclear Materials* 328, 77–87. <https://doi.org/10.1016/j.jnucmat.2004.05.001>
- Smallman, R.E., Ngan, A.H.W., 2007. Mechanical properties I, in: *Physical Metallurgy and Advanced Materials*. Butterworth-Heinemann, pp. 289–381.
- Song, B., Dong, S., Coddet, P., Liao, H., Coddet, C., 2014. Fabrication of NiCr alloy parts by selective laser melting: Columnar microstructure and anisotropic mechanical behavior. *Materials & Design* 53, 1–7. <https://doi.org/10.1016/j.matdes.2013.07.010>
- Srinivas, M., Babu, B.S., 2017. A Critical Review on Recent Research Methodologies in Additive Manufacturing. *Materials Today: Proceedings, International Conference on Advancements in Aeromechanical Materials for Manufacturing (ICAAMM-2016): Organized by MLR Institute of Technology, Hyderabad, Telangana, India* 4, 9049–9059. <https://doi.org/10.1016/j.matpr.2017.07.258>
- Steinmetz, D.R., Jäpel, T., Wietbrock, B., Eisenlohr, P., Gutierrez-Urrutia, I., Saeed–Akbari, A., Hickel, T., Roters, F., Raabe, D., 2013. Revealing the strain-hardening behavior of twinning-induced

- plasticity steels: Theory, simulations, experiments. *Acta Materialia* 61, 494–510. <https://doi.org/10.1016/j.actamat.2012.09.064>
- Tremsin, A.S., Gao, Y., Makinde, A., Bilheux, H.Z., Bilheux, J.C., An, K., Shinohara, T., Oikawa, K., 2021. Monitoring residual strain relaxation and preferred grain orientation of additively manufactured Inconel 625 by in-situ neutron imaging. *Additive Manufacturing* 46, 102130. <https://doi.org/10.1016/j.addma.2021.102130>
- ULM, K., 1990. SIMPLE METHOD TO CALCULATE THE CONFIDENCE INTERVAL OF A STANDARDIZED MORTALITY RATIO (SMR). *American Journal of Epidemiology* 131, 373–375. <https://doi.org/10.1093/oxfordjournals.aje.a115507>
- Vieille, B., Keller, C., Mokhtari, M., Briatta, H., Breteau, T., Nguejio, J., Barbe, F., Ben Azzouna, M., Baustert, E., 2020. Investigations on the fracture behavior of Inconel 718 superalloys obtained from cast and additive manufacturing processes. *Materials Science and Engineering: A* 790, 139666. <https://doi.org/10.1016/j.msea.2020.139666>
- Wang, Yin, Wang, Yue-ting, Li, R., Niu, P., Wang, M., Yuan, T., Li, K., 2021. Hall-Petch relationship in selective laser melting additively manufactured metals: using grain or cell size? *J. Cent. South Univ.* 28, 1043–1057. <https://doi.org/10.1007/s11771-021-4678-x>
- Wang, Y.M., Voisin, T., McKeown, J.T., Ye, J., Caltà, N.P., Li, Z., Zeng, Z., Zhang, Y., Chen, W., Roehling, T.T., Ott, R.T., Santala, M.K., Depond, P.J., Matthews, M.J., Hamza, A.V., Zhu, T., 2018. Additively manufactured hierarchical stainless steels with high strength and ductility. *Nature Mater* 17, 63–71. <https://doi.org/10.1038/nmat5021>
- Wilcox, B.A., Clauer, A.H., 1972. The role of grain size and shape in strengthening of dispersion hardened nickel alloys. *Acta Metallurgica* 20, 743–757. [https://doi.org/10.1016/0001-6160\(72\)90103-4](https://doi.org/10.1016/0001-6160(72)90103-4)
- Wolf, K., Gudladt, H.-J., Calderon, H.A., Kostorz, G., 1994. Transition between planar and wavy slip in cyclically deformed short-range ordered alloys. *Acta Metallurgica et Materialia* 42, 3759–3765. [https://doi.org/10.1016/0956-7151\(94\)90441-3](https://doi.org/10.1016/0956-7151(94)90441-3)
- Yun, C.-S., Hanawa, T., Hong, M.-H., Min, B.K., Kwon, T.-Y., 2021. Biocompatibility of Ni–Cr alloys, with the same composition, prepared by two new digital manufacturing techniques. *Materials Letters* 305, 130761. <https://doi.org/10.1016/j.matlet.2021.130761>
- Zhang, X.X., Knoop, D., Andrä, H., Harjo, S., Kawasaki, T., Lutz, A., Lahres, M., 2021. Multiscale constitutive modeling of additively manufactured Al–Si–Mg alloys based on measured phase stresses and dislocation density. *International Journal of Plasticity* 140, 102972. <https://doi.org/10.1016/j.ijplas.2021.102972>
- Zhang, X.X., Lutz, A., Andrä, H., Lahres, M., Gong, W., Harjo, S., Emmelmann, C., 2022. Strain hardening behavior of additively manufactured and annealed AlSi3.5Mg2.5 alloy. *Journal of Alloys and Compounds* 898, 162890. <https://doi.org/10.1016/j.jallcom.2021.162890>
- Zhang, Y.J., Han, D., Li, X.W., 2020. A unique two-stage strength-ductility match in low solid-solution hardening Ni–Cr alloys: Decisive role of short range ordering. *Scripta Materialia* 178, 269–273. <https://doi.org/10.1016/j.scriptamat.2019.11.049>
- Zhang, Z., Qu, Z., Xu, L., Liu, R., Zhang, P., Zhang, Zhefeng, Langdon, T.G., 2022. A general physics-based hardening law for single phase metals. *Acta Materialia* 231, 117877. <https://doi.org/10.1016/j.actamat.2022.117877>
- Zhao, C., Wang, Z., Li, D., Kollo, L., Luo, Z., Zhang, W., Prashanth, K.G., 2021. Selective laser melting of Cu–Ni–Sn: A comprehensive study on the microstructure, mechanical properties, and deformation behavior. *International Journal of Plasticity* 138, 102926. <https://doi.org/10.1016/j.ijplas.2021.102926>
- Zhao, Y., Meng, F., Liu, C., Tan, S., Xiong, W., 2021. Impact of homogenization on microstructure-property relationships of Inconel 718 alloy prepared by laser powder bed fusion. *Materials Science and Engineering: A* 826, 141973. <https://doi.org/10.1016/j.msea.2021.141973>
- Zhong, Y., Liu, L., Wikman, S., Cui, D., Shen, Z., 2016. Intragranular cellular segregation network structure strengthening 316L stainless steel prepared by selective laser melting. *Journal of Nuclear Materials* 470, 170–178. <https://doi.org/10.1016/j.jnucmat.2015.12.034>

